

Quarterly Technical Report

Solid State Research

1986:3

Lincoln Laboratory

MASSACHUSETTS INSTITUTE OF TECHNOLOGY

LEXINGTON, MASSACHUSETTS



Prepared under Electronic Systems Division Contract F19628-85-C-0002.

Approved for public release; distribution unlimited.

A04178394

The work reported in this document was performed at Lincoln Laboratory, a center for research operated by Massachusetts Institute of Technology, with the support of the Department of the Air Force under Contract F19628-85-C-0002.

This report may be reproduced to satisfy needs of U.S. Government agencies.

The views and conclusions contained in this document are those of the contractor and should not be interpreted as necessarily representing the official policies, either expressed or implied, of the United States Government.

The ESD Public Affairs Office has reviewed this report, and it is releasable to the National Technical Information Service, where it will be available to the general public, including foreign nationals.

This technical report has been reviewed and is approved for publication.

FOR THE COMMANDER

Thomas J. Alpert, Major, USAF
Chief, ESD Lincoln Laboratory Project Office

Non-Lincoln Recipients

PLEASE DO NOT RETURN

Permission is given to destroy this document
when it is no longer needed.

**MASSACHUSETTS INSTITUTE OF TECHNOLOGY
LINCOLN LABORATORY**

SOLID STATE RESEARCH

QUARTERLY TECHNICAL REPORT

1 MAY — 31 JULY 1986

7 JANUARY 1987

Approved for public release; distribution unlimited.

LEXINGTON

MASSACHUSETTS

ABSTRACT

This report covers in detail the solid state research work of the Solid State Division at Lincoln Laboratory for the period 1 May through 31 July 1986. The topics covered are Solid State Device Research, Quantum Electronics, Materials Research, Microelectronics, and Analog Device Technology. Funding is provided primarily by the Air Force, with additional support provided by the Army, DARPA, Navy, SDIO, NASA, and DOE.

TABLE OF CONTENTS

Abstract	iii
List of Illustrations	vii
List of Tables	xi
Introduction	xiii
Reports on Solid State Research	xv
Organization	xxiii
 1. SOLID STATE DEVICE RESEARCH	 1
1.1 High-Speed Photoconductive Switches Fabricated on Ti-Doped Semi-insulating InP	1
1.2 Diode Lasers with Cylindrical Mirror Facets	7
 2. QUANTUM ELECTRONICS	 13
2.1 Ti:Al ₂ O ₃ Laser Development	13
2.2 Electro-optic Tuning of a Ti:Al ₂ O ₃ Laser	15
2.3 Er:YAG Laser Development	17
2.4 Laser Frequency Conversion	19
 3. MATERIALS RESEARCH	 23
3.1 Tracer Gas Studies for OMVPE Reactor Design	23
3.2 Radiation Effects on CMOS Circuits Fabricated in SOI Films	25
 4. MICROELECTRONICS	 33
4.1 MBE-Grown Insulating GaAs Used as MESFET Buffers	33
4.2 Charge-Coupled Device Imagers	33
4.3 Wafer Thinning Process	36
4.4 Attainment of 0.13- μ m Lines and Spaces by Excimer-Laser Projection Lithography	38
4.5 Observation of Millimeter-Wave Oscillations from Resonant- Tunneling Diodes and Some Theroretical Considerations of Oscillation-Frequency Limits	39

5. ANALOG DEVICE TECHNOLOGY	45
5.1 High-Performance Superconductive Chirp Filters	45
5.2 Superconductive Delay Line with Integral MOSFET Taps	50
5.3 Further Assessment of Nonlinear Associative Memory for Detecting Lines in Images	52

LIST OF ILLUSTRATIONS

Figure No.		Page
1-1	Schematic of Device Structure and Photomicrograph of Electrode Geometry	2
1-2	Typical I-V Characteristics for Ti-Doped InP Switches Under Uniform Illumination of 1, 3, and 5 mW	3
1-3	Effect on I-V Characteristics of Position of Laser Spot Between Electrodes. Hysteresis Is Due to Curve Tracer. Notice Different Vertical Scales for the Two Series	4
1-4	Response of Ti- and Fe-Doped InP Switches to a 40-ps Optical Pulse	5
1-5	Waveforms and Reference Conditions for Step-Bias Measurements and Expected Switch Response (Not to Scale)	6
1-6	Response to Optical Pulse and Step-Bias for (a) Fe-Doped, and (b) Ti-Doped InP Switches. Top to Bottom Are Electrical Bias, Optical Input Pulse, Switch Output Under Illumination, and Switch Output in the Dark (Showing Capacitive Feedthrough)	7
1-7	Schematic Top View of Wafer Showing a Cylindrical Mirror Facet and a Typical Cleavage Plane that, at Opposite Ends of the BH Mesa Section, Form the Laser Cavity	8
1-8	Radiation Patterns Obtained from Each End of a Laser Operating in the Lowest-Order Lateral Mode. The FWHM Angles Are 9.2° and 40° for the Cylindrical and Cleaved Facets, Respectively	9
1-9	Radiation Patterns Obtained from Each End of a Laser Operating in a Second-Order Lateral Mode. The Angles Between the Dominant Lobes Are Indicated	9
2-1	Threshold Pump Power P_{th} for a Ti:Al ₂ O ₃ Laser as a Function of Temperature. The Circles Represent the Data Points and the Curve Represents the Predicted Variation Based on the Known Temperature Dependence of the Total Relaxation Rate, γ_t	13
2-2	Spontaneous Fluorescence Intensity for a Ti:Al ₂ O ₃ Laser as a Function of Temperature. The Circles Represent the Data Points and the Curve Represents the Predicted Variation Assuming That Only the Nonradiative Relaxation Rate γ_{nr} Is Temperature Dependent	14

Figure No.		Page
2-3	Spontaneous Fluorescence Spectra for the Ti:Al ₂ O ₃ Laser Recorded When the Laser Is (a) Off, (b) On, and (c) at Threshold. The Spike at λ_L Is Due to Scattered Radiation from the Laser	14
2-4	Principle of Operation of the Electro-optic Filter. For the Device Described in the Text, $d = 1$ mm, $L = 25$ mm	15
2-5	Cavity Layout of the Electro-optically Tuned Ti:Al ₂ O ₃ Laser	16
2-6	Static Tuning Curves of the Ti:Al ₂ O ₃ Laser	17
2-7	Energy Level Diagram for Er:YAG	18
2-8	Experimental Arrangement for Second Harmonic Generation at $1.65 \mu\text{m}$	19
2-9	(a) Simultaneous Oscilloscope Traces of Laser Input to KTP Crystal at Fundamental Frequency ω and Second Harmonic 2ω , (b) Second Harmonic Efficiency as a Function of Laser Input Power Density	21
3-1	Time Dependence of C/C_0 , Where C Is the SF ₆ Concentration Measured at the Susceptor of a Vertical Reactor Tube and C_0 Is the Initial Concentration in the Gas Stream, for SF ₆ Flow Switched On at $t = 0$ and Switched Off at $t = 60$ s. Inlet-to-Susceptor Distance: (a) 16 cm, (b) 4 cm	24
3-2	Time Dependence of C/C_0 for SF ₆ Flow Switched On and Off at Intervals of 18 s. Inlet-to-Susceptor Distance: (a)-(c) 16 cm, (d)-(f) 4 cm	26-27
3-3	Photograph of a 1.2-K SOI/CMOS Gate Array	28
3-4	Photograph of a 1-K SOI/CMOS SRAM	28
3-5	Threshold Voltages of SOI/CMOS Devices as a Function of Total Dose	31
4-1	Abutted Four-Chip Imager Mosaic	34
4-2	Assembly of Four-Chip Array	35
4-3	Completed Four-Chip Array	36
4-4	140X Photograph Showing the Point Defects Caused by Oxygen Precipitation in the Bulk	37
4-5	780X Photograph Showing Shallow Etch Pits on the Epitaxial Layer Due to the Point Defects in the Bulk	37
4-6	SEMs Taken at Two Different Magnifications, of $0.13\text{-}\mu\text{m}$ Lines and Spaces on Carbon Resist on GaAs (One 193-nm pulse, $\sim 0.2 \text{ J/cm}^2$ Fluence)	39
4-7	Current-Voltage Curve of Double-Barrier Diode	40

Figure No.		Page
5-1	Insertion Loss vs Frequency of a Flat-Weighted Superconductive Chirp Filter	46
5-2	Phase Error (Deviation from Best-Fit Quadratic) of a Flat-Weighted Superconductive Chirp Filter	46
5-3	Insertion Loss vs Frequency of a Hamming-Weighted Superconductive Chirp Filter	47
5-4	Phase Error (Deviation from Best-Fit Quadratic) of a Hamming-Weighted Superconductive Chirp Filter	48
5-5	Compressed-Pulse Response of Matched Flat- and Hamming-Weighted Superconductive Chirp Filters	48
5-6	Compressed Pulse Response Envelope Generated from Amplitude and Phase Data of Same Devices as in Figure 5-5	49
5-7	Mask Layout of the Programmable Tapped Delay Line Showing Transmission Line, Taps, and Transistors. The Niobium Areas Are Filled and the Aluminum Areas Are Open. The Large Aluminum Capacitors Attached to Four of the Transistors Are Bypass Capacitors to Ground to Reduce Feedthrough	50
5-8	Normalized Insertion Gain Measurements vs Frequency, Plotted for Three Different Gate Voltages. The Curves Plotted Are Normalized to the Measurement at -8 V. The MOSFET Controlling This Tap Does Not Have Gate Bypassing	51
5-9	Measurement of the Modulated Channel Conductance as a Function of Gate Voltage for a Tap Controlled by a Non-Gate-Bypassed Nb-Gate Transistor	52
5-10	Hopfield Memory	53
5-11	Recognition of (a) No-Line and (b) Line Patterns in 9-by-9 Images Using Various Processors: (1) Unmodified Hopfield, (2) Hopfield with Orthonormal Basis Vectors, (3) Orthonormal Basis Vectors and Analog Processing on First Pass, (4) Matched Filter, and (5) Hopfield with Orthonormal Basis Vectors and Analog Processing Using an Offset Sigmoid Nonlinear Operator	54
5-12	Line-Detector Performance for 5-by-5 Images at +6-dB Input SNR with (a) Random Additive Errors in the Processor Coefficients, and (b) Random Dropouts of Processor Elements. The Curves Show Averages over Many Processor Error Patterns	55

LIST OF TABLES

Table No.		Page
3-1	Comparison of ZMR and SIMOX CMOS Device Characteristics	29
3-2	Comparison of ZMR and SIMOX Circuit Performance	29
3-3	Total-Dose Failure Threshold for ZMR and SIMOX Circuits	32
4-1	Resonant Tunneling Diode Parameters	41

INTRODUCTION

1. SOLID STATE DEVICE RESEARCH

Optoelectronic switches have been fabricated on bulk semi-insulating InP produced by compensating Zn-doped p-type InP with Ti. These switches show response times in the range of 60 ps, which is considerably faster than observed for similar switches made on Fe-doped InP. In addition, charge storage effects, which have been a serious problem in sample-and-hold circuit applications, were found to be an order of magnitude less for Ti-doped InP switches than for the Fe-doped InP switches.

Diode laser mirrors have been fabricated that are circularly curved in the junction plane. The curvature is designed to provide good reflective feedback and to form output lenses that reduce the divergence of the output laser beams. Low threshold current (25 mA) lasers were achieved with over a factor of three reduction in output beam divergence.

2. QUANTUM ELECTRONICS

A Ti:Al₂O₃ laser has been operated CW at temperatures up to 120°C. The threshold pump power increases with temperature because of the increase in nonradiative relaxation rate. It has been shown that the fluorescence transition responsible for the laser action is homogeneously broadened.

A transverse-effect LiNbO₃ modulator has been employed successfully to tune a Ti:Al₂O₃ laser across most of its gain bandwidth. Optical damage in the LiNbO₃ is not a problem provided the Ar-laser pump light is spatially separated from the infrared laser beam.

Laser operation at 1.65 μ m in Er:YAG is limited to temperatures less than 160 K; this limitation may be related to a parasitic upconversion process. The parasitic upconversion acts as a loss mechanism for the I_{13/2} excited state population density and may preclude the use of Er:YAG as an efficient diode-pumped laser system.

Second harmonic generation experiments with KTP and LiIO₃ indicate that presently available KTP crystals are not suitable for the frequency-doubling phase of tripling 1.65- μ m radiation, while the use of LiIO₃ remains a possibility. A new long-pulse Nd:YAG laser has been used for frequency-doubling efficiency measurements for KTP.

3. MATERIALS RESEARCH

To obtain data for optimizing the design of a reactor for growing GaAs/AlGaAs layers by organometallic vapor phase epitaxy, the passage of process gases through a vertical reactor tube has been investigated by tracer gas experiments in which the concentration of gaseous SF₆ at the susceptor disk is measured as a function of time after the flow of SF₆ into the carrier gas stream is switched on or off. The abruptness of the change in this concentration, which should be correlated with the abruptness of the interfaces between successive epitaxial layers, can be increased significantly

by increasing the carrier gas velocity and decreasing the distance between the susceptor and the gas inlet.

Fully functional CMOS 1 K static random-access memories and 1.2 K gate arrays have been fabricated with good yields in silicon-on-insulator films prepared by zone-melting recrystallization and by oxygen ion implantation. Excellent transient-radiation resistance has been demonstrated for both types of memories, which showed no logic upset for dose rates up to 7×10^{10} rad/s.

4. MICROELECTRONICS

A new process has been developed for growing buffer layers for GaAs MESFETs by low temperature MBE. This process shows great promise in reducing device sensitivity to light and leakage currents and in increasing source-drain breakdown voltage.

A technique has been developed for the precision assembly of four charge-coupled device (CCD) imagers into a 2×2 focal plane array. Each CCD consists of 420×420 pixels and abuts other imagers along two adjacent edges. The chips can be positioned with less than $1\text{-}\mu\text{m}$ misalignment within the plane of the CCDs and are mutually coplanar to within $3\text{ }\mu\text{m}$.

A wafer thinning process for backside illuminated CCDs has been developed, using a combination of lapping, polishing, and selective etching. The etch stops with good selectivity on the epitaxial layer. Shallow etch pits in the final etched surface have been shown to be related to oxygen precipitates in the bulk silicon substrate, which is etched away.

'Diamond-like' hard carbon film was used as a photoresist for excimer-laser projection lithography. Well resolved $0.13\text{-}\mu\text{m}$ lines and spaces have been achieved using 193-nm radiation and reflective optics.

Oscillation frequencies as high as 56 GHz have been observed from resonant-tunneling double-barrier diodes. Recent theoretical considerations yield a maximum oscillation frequency of several hundred gigahertz.

5. ANALOG DEVICE TECHNOLOGY

Improvements in the fabrication and packaging processes have led to high-performance superconductive chirp filters with rms phase errors of less than 6° across the full 2.6-GHz bandwidth of the 37.5-ns-long devices. Pulse-compression measurements have demonstrated relative side-lobe levels of -29 dB , in good agreement with the design value of -30 dB .

A superconducting tapped delay line with programmable MOS transistors for tap weights has been designed, fabricated, and tested at 4.2 K. Test results show that the amplitude of the tapped outputs may be varied linearly over an 18-dB range, between 2 and 2.4 GHz, by gate-voltage modulation of the MOSFET channel conductance.

An analysis of a nonlinear associative memory for detecting lines in noisy images has been extended to 9×9 -pixel fields. With the use of a variable-steepness arctangent nonlinearity, the detection performance approaches that of a matched filter, but the latter exhibits superior tolerance to faults in the coefficient values stored in the processor.

REPORTS ON SOLID STATE RESEARCH

1 May through 31 July 1986

PUBLISHED REPORTS

Journal Articles

JA No.

5300	II-VI and IV-VI Semiconductors	A.J. Strauss	In <i>Encyclopedia of Materials Science and Engineering</i> , M.B. Bever, Ed. (Pergamon Press, Oxford, 1986), p. 4341
5505A	Limitations on Power Transfer Efficiency in Three-Guide Optical Couplers	J.P. Donnelly	IEEE J. Quantum Electron. QE-22 , 610 (1986)
5767	Double-Heterostructure InGaAsP/InP PIN Photodetectors	V.Diadiuk S.H. Groves	Solid-State Electron. 29 , 229 (1986), DTIC AD-A167365
5831	You Too Can Present a Paper	D.L. Hovey R. Ponton*	Fusion — The Journal of the American Scientific Glassblowers Society 33 , 52 (1986)
5832	Radiation-Hardened Silicon-on-Insulator Complementary Junction Field-Effect Transistors	B-Y. Tsaur H.K. Choi	IEEE Electron Device Lett. EDL-7 , 324 (1986)
5834	New Capping Technique for Zone-Melting Recrystallization of Silicon-on-Insulator Films	C.K. Chen M.W. Geis M.C. Finn B-Y. Tsaur	Appl. Phys. Lett. 48 , 1300 (1986)
5837	Electronic Structure of Deep-Lying Sulfur Centers in Si	W.E. Krag W.H. Kleiner* H.J. Zeiger	Phys. Rev. B 33 , 8304 (1986)
5841	Thoughts on the Junction Laser: The Past and the Future	R.H. Rediker	Optoelectronics OP-DET 1 , 102 (1986)

* Author not at Lincoln Laboratory.

JA No.

- | | | | |
|------|---|---|--|
| 5845 | Magnetic and Optical Measurements on Ti:Al ₂ O ₃ Crystals for Laser Applications: Concentration and Absorption Cross Section of Ti ³⁺ Ions | R.L. Aggarwal
A. Sanchez
R.E. Fahey
A.J. Strauss | Appl. Phys. Lett. 48 , 1345 (1986) |
| 5846 | Room-Temperature Continuous-Wave Operation of a Ti:Al ₂ O ₃ Laser | A. Sanchez
R.E. Fahey
A.J. Strauss
R.L. Aggarwal | Opt. Lett. 11 , 363 (1986) |
| 5848 | Titanium-Doped Semi-insulating InP Grown by the Liquid-Encapsulated Czochralski Method | G.W. Iseler
B.S. Ahern* | Appl. Phys. Lett. 48 , 1656 (1986) |
| 5851 | Monolithic Two-Dimensional Arrays of High-Power GaInAsP/InP Surface-Emitting Lasers | J.N. Walpole
Z.L. Liao | Appl. Phys. Lett. 48 , 1636 (1986) |
| 5856 | Monolithic GaAs/AlGaAs Diode Laser/Deflector Devices for Light Emission Normal to the Surface | T.H. Windhorn
W.D. Goodhue | Appl. Phys. Lett. 48 , 1675 (1986) |
| 5863 | Submicrometer CMOS Devices in Zone-Melting-Recrystallized SOI Films | B-Y. Tsaur
C.K. Chen | IEEE Electron Device Lett. EDL-7 , 443 (1986) |

Meeting Speeches**MS No.**

- | | | | |
|------|--|----------------------------|--|
| 6961 | Autocalibrating Circuitry for Processing Saw Convolver Outputs | J.H. Fischer | In <i>1985 Ultrasonics Symposium Proceedings</i> (IEEE, New York, 1985), pp. 134-139 |
| 7096 | Spectral Linewidth of Semiconductor Lasers | J.Harrison
A. Mooradian | <i>Methods of Laser Spectroscopy</i> , edited by Y. Prior, A. Ben-Reuven, and M. Rosenbluh (Plenum Press, New York, 1986), pp. 133-142 |

* Author not at Lincoln Laboratory.

MS No.

7102 Saw Convolvers and Signal
Processing in a Packet Radio

J.H. Fischer
J. Cafarella
G.T. Flynn

In 1986 *IEEE-MTT-S
International Microwave
Symposium Digest*,
Baltimore, Maryland,
2-4 June 1986

* * * * *

UNPUBLISHED REPORTS**Journal Articles****JA No.**

5864 A Technology for Optical
Interconnection Based on
Multichip Integration

D.Z. Tsang
D.L. Smythe
A. Chu
J.J. Lambert

Accepted by Optical
Engineering

5865 Monolithic Integration of
GaAs/AlGaAs Double-
Heterostructure LED's and
Si MOSFET's

H.K. Choi
G.W. Turner
T.H. Windhorn
B-Y. Tsaur

Accepted by Electron Device
Lett.

5882 Wideband Packet Radio
Technology

J.H. Fischer
J.H. Cafarella
D.R. Arsenault
G.T. Flynn
C.A. Bouman

Accepted by Proc. IEEE

Meeting Speeches***MS No.**

6922 Permeable Base Transistor

C.O. Bozler

7119 The Design of GaAs Monolithic
Circuits for Magnetostatic Wave
Delay Lines

C.L. Chen
A. Chu†
L.J. Mahoney
W.E. Courtney
J.C. Sethares†

1986 IEEE Microwave &
M. Wave Monolithic
Circuit Symposium,
2-4 June 1986,
Baltimore, Maryland

* Titles of Meeting Speeches are listed for information only. No copies are available for distribution.

† Author not at Lincoln Laboratory.

MS No.

7019A	Silicon-on-Insulator Technologies for Integrated-Circuit Applications	B-Y. Tsaur	}	169th Meeting of the Electrochemical Society, Boston, Massachusetts, 4-9 May 1986
7083	A New Capping Technique for Zone-Melting Recrystallization of SOI	C.K. Chen M.W. Geis B-Y. Tsaur M.C. Finn		
7021A	Linewidth Reduction of Semiconductor Diode Lasers	J. Harrison A. Mooradian		Seminar, Allied Corporation, Mt. Bethel, New Jersey, 20 June 1986
7049	Growth of Laser-Quality Ti:Al ₂ O ₃ Crystals by a Seeded Gradient-Freeze Technique	R.E. Fahey A.J. Strauss A.Sanchez R.L. Aggarwal		8th International Conference on Crystal Growth, York, Yorkshire, United Kingdom, 13-18 July 1986
7104	Room-Temperature cw Operation of a Ti:Al ₂ O ₃ Laser	A. Sanchez R.E. Fahey A.J. Strauss R.L. Aggarwal	}	CLEO '86, San Francisco, California, 9-13 June 1986
7106	Monolithic Two-Dimensional Arrays of High-Power GaInAsP/InP Surface-Emitting Lasers	J.N. Walpole Z.L. Liao		
7124	Small-Signal Modulation of P-Substrate Mass-Transported GaInAsP/InP Lasers	D.Z. Tsang Z.L. Liao		
7148	Picosecond Carrier Density Dynamics of a Modulated GaAlAs Diode Laser	B.C. Johnson A. Mooradian		
7161	Laser-Direct-Written Interconnects: Applications to Real-World Circuits	J.G. Black S.P. Doran D.J. Ehrlich		
7104A	Room-Temperature cw Operation of a Ti:Al ₂ O ₃ Laser	A. Sanchez R.E. Fahey A.J. Strauss R.L. Aggarwal	}	Topical Meeting on Tunable Solid State Lasers, Zigzag, Oregon, 4-6 June 1986
7160	Growth of Ti:Al ₂ O ₃ Crystals by a Gradient-Freeze Technique	R.E. Fahey A.J. Strauss A. Sanchez		

MS No.

7123	Bulk Acoustic-Wave Reflection-Grating Devices in Fe:LiNbO ₃	D.E. Oates J.Y. Pan	International Symposium on the Application of Ferroelectrics, Bethlehem, Pennsylvania, 8-11 June 1986
7124A	Small-Signal Modulation of P-Substrate Mass-Transported GaInAsP/InP Lasers	D.Z. Tsang Z.L. Liao	Workshop on Microwave Aspects of GHz/Gbit Optical Transmission Systems, Baltimore, Maryland, 5 June 1986
7125	High-Speed Optical Interconnects Using Multichip Integration	D.Z. Tsang D.L. Smythe J.J. Lambert	
7124B	Small-Signal Modulation of P-Substrate Mass-Transported GaInAsP/InP Lasers	D.Z. Tsang Z.L. Liao	Third International Workshop on Semiconductor Lasers, San Francisco, California, 7 June 1986
7126	Growth of GaAs on Si	G.W. Turner	1986 AIME Northeast Regional Meeting, Murray Hill, New Jersey, 1-2 May 1986
7127	Electron-Beam Programming and Testing of CMOS Systems	T.M. Lyszczarz S. Oliver M. Paczuski J. Freed*	30th Symposium on EIPB, Boston, Massachusetts, 27-30 May 1986
7138	Masked Ion Beam Lithography for Submicrometer-Gate- Length Transistors	S.W. Pang T.M. Lyszczarz C.L. Chen J.P. Donnelly J.N. Randall	
7141	Visible-Laser Photochemical Etching of Molybdenum and Tungsten	M. Rothschild J.H.C. Sedlacek J.G. Black D.J. Ehrlich	
7142	Direct Writing of Silicon and Tungsten Interconnects by Laser Deposition and Applications to Microcircuitry	J.G. Black D.J. Ehrlich S.P. Doran J.H.C. Sedlacek	

* Author not at Lincoln Laboratory.

MS No.

7143	Hot Jet Etching of Si With SF ₆ and Pb with n-Butane	M.W. Geis N.N. Efremow, Jr. S.P. Pang A.C. Anderson	30th Symposium on EIPB, Boston, Massachusetts, 27-30 May 1986
7144A	Methods and Materials for Submicrometer-Resolution Excimer-Laser Projection Patterning	D.J. Ehrlich M. Rothschild	
7155	Cermet as an Inorganic Resist for Ion Lithography	J. Melngailis D.J. Ehrlich J.N. Randall S.W. Pang	
7135A	Picosecond Characterization of the Permeable Base Transistor Using Electro-optic Sampling	D.R. Dykaar* G.A. Mourou* M.A. Hollis B.J. Clifton K.B. Nichols C.O. Bozler R.A. Murphy	5th Topical Meeting on Ultrafast Phenomena, Aspen, Colorado, 16-19 June 1986
7143A	Hot Jet Etching of Si with SF ₆ and Pb with n-Butane	M.W. Geis N.N. Efremow, Jr. A.C. Anderson	Gordon Conference, Wolfeboro, New Hampshire, 7-11 July 1986
7149	Radiation-Hardened JFET Devices and CMOS Circuits in Zone-Melting-Recrystallized SOI Films	B-Y. Tsaur V.J. Sferriano H.K. Choi C.K. Chen R.W. Mountain J.T. Schott* W.M. Shedd* D.C. LaPierre* R. Blanchard	23rd Annual Conference on Nuclear and Space Radiation Effects, Providence, Rhode Island, 21-23 July 1986
7150	Flow Visualization and Tracer GaAs Studies for Optimization of OMVPE Reactor Design	C.A. Wang D.W. Weyburne* R.A. Brown* S.H. Groves S.C. Palmateer	1986 Electronic Materials Conference, University of Massachusetts, Amherst, Massachusetts, 25-27 June 1986
7157	Titanium-Doped Semi-Insulating InP Grown by the Liquid-Encapsulated Czochralski Method	G.W. Iseler B.S. Ahern*	

* Author not at Lincoln Laboratory.

MS No.

7164	Monolithic Integration of GaAs/AlGaAs Double-Heterostructure LEDs and Si MOSFETs	H.K. Choi G.W. Turner T.H. Windhorn B-Y. Tsaur	44th Annual Device Research Conference, University of Massachusetts, Amherst, Massachusetts, 23-25 June 1986
7172	Millimeter-Band Oscillations in a Resonant-Tunneling Device	E.R. Brown T.C.L.G. Sollner W.D. Goodhue P.E. Tannenwald B.J. Clifton	
7195	High-Speed, High-Sensitivity Photoconductive Switches Fabricated on Ti-Doped Semi-insulating InP	V. Diadiuk G.W. Iseler G.A. Ferrante C.H. Cox, III	
7197	Comparison of CMOS Devices and Circuits Fabricated in Zone-Melting-Recrystallized SOI, Implanted Buried-Oxide SOI, and SOS Substrates	B-Y. Tsaur C.K. Chen R.W. Mountain	
7174	Early Applications of Laser Direct Patterning: Direct Writing and Excimer Projection	D.J. Ehrlich	European MRS Meeting, Strasbourg, France, 17 June 1986
7196	Materials Aspects of Heteroepitaxy of GaAs on Si	S.J. Eglash	New England Combined Chapter of the American Vacuum Society, Nashua, New Hampshire, 9-11 June 1986
7208	A Comparison of Nonlinear Associative Memory and Matched Filter Processing for Detecting Lines in Images	P.M. Grant J.P. Sage	Seminar, BBN Laboratories, Cambridge, Massachusetts, 6 May 1986
7215	An Overview of Multiple Quantum Well Structures: Physics and Applications	B.F. Aull	Tutorial, Northeastern University, Boston, Massachusetts, 12 May 1986
7221	Advances in Far-Infrared Heterodyne Detectors	E.R. Brown P.E. Tannenwald	SPIE '86 Symposium on Optical and Optoelectronic Sciences, Quebec, Canada, 2-6 June 1986

MS No.

7227 The Fabrication and
Performance of the Permeable
Base Transistor

R.A. Murphy

Graduate Student Seminar,
Stanford University,
Stanford, California,
16 May 1986

7238 Optics for Computation

P.L. Kelley

7239 New Directions in Electronic
and Optical Technology

A.L. McWhorter

} Lax Symposium, Francis
Bitter National Magnet
Laboratory, Massachusetts
Institute of Technology,
Cambridge, Massachusetts,
23 May 1986

ORGANIZATION

SOLID STATE DIVISION

A.L. McWhorter, *Head*
I. Melngailis, *Associate Head*
E. Stern, *Associate Head*
J.F. Goodwin, *Assistant*

P.E. Tannenwald, *Senior Staff*
N.L. DeMeo, Jr., *Associate Staff*

QUANTUM ELECTRONICS

A. Mooradian, *Leader*
P.L. Kelley, *Associate Leader*

Barch, W.E.	Le, H.Q.
Belanger, L.J.	Menyuk, N.
Brailove, A.A.	Owen, R.L.
Daneu, V.	Sanchez-Rubio, A.
DeFeo, W.E.	Sharpe, K.A.
Feldman, B.	Sullivan, D.J.
Hancock, R.C.	Tong, F.F-K.*
Harrison, J.*	Wall, K.F.
Jeys, T.H.	Zayhowski, J.J.
Killinger, D.K.	

ELECTRONIC MATERIALS

A.J. Strauss, *Leader*
B-Y. Tsaur, *Assistant Leader*
H.J. Zeiger, *Senior Staff*

Anderson, C.H., Jr.	Kolesar, D.F.
Button, M.J.	Krohn, L., Jr.
Chen, C.K.	Mastromattei, E.L.
Choi, H.K.	Mattia, J.P.
Connors, M.K.	Nitishin, P.M.
Delaney, E.J.	Pantano, J.V.
Eglash, S.J.	Tracy, D.M.
Fahey, R.E.	Turner, G.W.
Finn, M.C.	Wang, C.A.
Iseler, G.W.	Windhorn, T.H.

APPLIED PHYSICS

R.C. Williamson, *Leader*
D.L. Spears, *Assistant Leader*
T.C. Harman, *Senior Staff*
R.H. Rediker, *Senior Staff*

Anderson, K.K.*	Hovey, D.L.	Plonko, M.C.
Aull, B.F.	Johnson, L.M.	Reeder, R.E.
Betts, G.E.	Liau, Z-L.	Tsang, D.Z.
Chan, S.K.*	Lind, T.A.	Walpole, J.N.
Cox, C.H., III	McBride, W.F.	Whitaker, N.*
Diadiuk, V.	Metze, G.M.	Woodhouse, J.D.
Donnelly, J.P.	Molter, L.A.*	Yap, D.*
Ferrante, G.A.	O'Donnell, F.J.	Yee, A.C.
Groves, S.H.	Palmateer, S.C.	

* Research Assistant

ANALOG DEVICE TECHNOLOGY

R.W. Ralston, *Leader*

R.S. Withers, *Assistant Leader*

Anderson, A.C.
Arsenault, D.R.
Boisvert, R.R.
Brogan, W.T.
Denneno, A.P.
DiIorio, M.S.
Dolat, V.S.
Fischer, J.H.
Fitch, G.L.

Flynn, G.T.
Grant, P.M.
Green, J.B.
Holtham, J.H.
Kernan, W.C.
Koulman, W.A.
Lattes, A.L.
Lichtenwalner, D.L.*
Macedo, E.M., Jr.

Macropoulos, W.
Marden, J.A.
Munroe, S.C.
Oates, D.E.
Sage, J.P.
Slattery, R.L.
Thompson, K.E.†
Wong, S.*

MICROELECTRONICS

W.T. Lindley, *Leader*

D.J. Ehrlich, *Assistant Leader*

B.B. Kosicki, *Assistant Leader*

R.A. Murphy, *Assistant Leader*

Astolfi, D.K.
Bales, J.W.*
Bennett, P.C.
Black, J.G.
Bozler, C.O.
Brown, E.R.
Burke, B.E.
Calawa, A.R.
Chen, C.L.
Chiang, A.M.
Clifton, B.J.
Cullen, P.A.*
Daniels, P.J.
Doran, S.P.
Durant, G.L.
Efremow, N.N., Jr.
Felton, B.J.
Gajar, S.A.

Geis, M.W.
Goodhue, W.D.
Gray, R.V.
Hollis, M.A.
Huang, J.C.M.
Johnson, K.F.
Lax, B.‡
LeCoz, Y.L.*
Lincoln, G.A., Jr.
Lyszczarz, T.M.
Mahoney, L.J.
Maki, P.A.
Manfra, M.J.
Mathews, R.H.
McGonagle, W.H.
Melngailis, J.‡
Mountain, R.W.
Nichols, K.B.

Oliver, S.
Paczuski, M.
Pang, S.W.
Parker, C.D.
Pichler, H.H.
Rabe, S.
Rathman, D.D.
Reinold, J.H., Jr.
Rothschild, M.
Sedlacek, J.H.C.
Smith, F.W.*
Smythe, D.L., Jr.
Sollner, T.C.L.G.
Taylor, J.A.*
Utarro, R.S.
Vera, A.
Wilde, R.E.
Young, E.M.

* Research Assistant

† Staff Associate

‡ Part Time

1. SOLID STATE DEVICE RESEARCH

1.1 HIGH-SPEED PHOTOCONDUCTIVE SWITCHES FABRICATED ON Ti-DOPED SEMI-INSULATING InP

Optoelectronic switches have been fabricated on bulk semi-insulating ($\rho \times 3.3 \times 10^6 \Omega\text{-cm}$) InP produced by compensating Zn-doped p-type InP with Ti. These Ti-doped switches show response times in the range of 60 ps, which is considerably faster than observed for similar switches made on Fe-doped InP. In addition, charge storage effects, which have been a serious problem in sample-and-hold circuit applications, were found to be an order of magnitude less for Ti-doped InP switches than for the Fe-doped InP switches.

In recent years, there has been great interest in photoconductive devices for use as optoelectronic switches, detectors, and mixers because of their relative ease of fabrication, speed of response and absence of cross-talk between the optical and electronic inputs. When such devices are fabricated on semi-insulating (SI) substrates, they offer the additional advantage of being easily integrated with other electronic or optical components.

Most of the work to date on InP photoconductive switches has been on Fe-doped material. These devices have shown high sensitivity (external quantum efficiencies on the order of 30% without antireflection coating) and response times ranging from several hundred picoseconds to a few nanoseconds, depending on the Fe concentration. However, some of the observed characteristics of the Fe-doped InP switches are not only undesirable, but also not well understood. The I-V characteristics are nonlinear, showing saturation at low bias voltages, and are strongly affected by the uniformity of illumination.¹ In addition, when the device is biased with a step voltage (conditions present in a sample-and-hold circuit),² a large excess capacitive-like feedthrough occurs. These effects appear to be related to the absence of ohmic contacts (inherent in material with the Fermi level near the center of the bandgap) and the Fe impurities, which are deep acceptors that tend to capture electrons.

The purpose of the current work was to try to gain greater understanding of the physics of these SI InP switches by studying Ti-doped InP,³ whose impurity states are deep donors. The resistivity of Fe-doped InP is about 100 times that of Ti-doped InP, but both materials exhibit bulk mobilities of about $2500 \text{ cm}^2/\text{V-s}$ and our measurements are not particularly sensitive to dark resistivity values.

The device structure investigated is shown in Figure 1-1 and consists of a wafer of either Ti- or Fe-doped InP with either evaporated Au or evaporated and alloyed (420°C for 20 s) NiGeAu electrodes. The photoconductors had either a single gap of 3, 5, or $10 \mu\text{m}$, or interdigitated electrodes with 2-, 4- or $6\text{-}\mu\text{m}$ finger widths and spacings. All devices exhibit essentially the same behavior, regardless of electrode composition or geometry. After fabrication, the individual chips were cleaved and mounted in a high-speed microstrip transmission-line package, in which the chip itself constituted the only departure from 50 ohms.

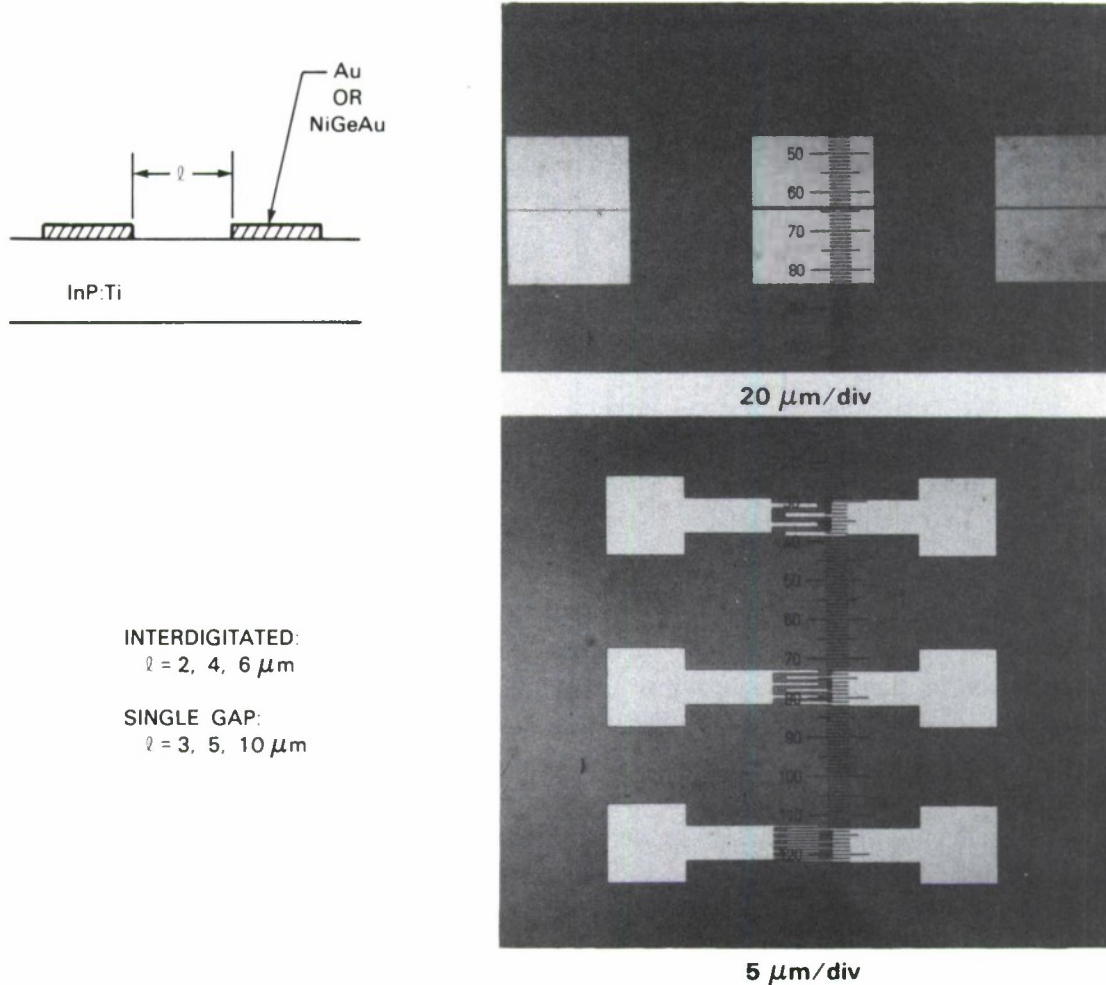


Figure 1-1. Schematic of device structure and photomicrograph of electrode geometry.

Typical I-V characteristics under uniform illumination levels of 1, 3, and 5 mW are shown in Figure 1-2 for a 4- μm -gap interdigitated-electrode Ti-doped device. At low bias, the I-V characteristics are linear. In this region, the Ti-doped switches have higher photoconductance than similar Fe-doped devices, indicating a longer photoconductive lifetime or higher effective mobility for the Ti-doped material. At higher bias, there is a quasi-saturation in the I-V characteristics, with the knee of the I-V curve occurring at about 200 mV for this particular device. Knee voltages have ranged from less than 200 mV to about 1 V in the Ti-doped devices. The photocurrent saturation is more abrupt and occurs at a lower bias in Ti-doped InP switches than in similar Fe-doped InP switches. However, while the photocurrent is proportional to the incident optical power in Fe-doped devices, some superlinear behavior is observed in Ti-doped switches. From the value of the photocurrent at the knee for an incident optical power of 3 mW,

we obtain a responsivity of about 0.2 A/W when corrected for shadowing due to the electrodes. This responsivity is close (within a factor of two) to the value expected for an internal quantum efficiency of unity at a photoconductive gain of one.

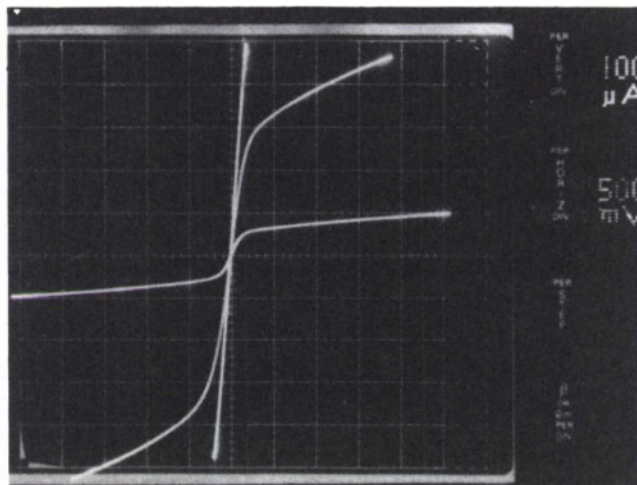


Figure 1-2. Typical I-V characteristics for Ti-doped InP switches under uniform illumination of 1, 3, and 5 mW.

As has been reported previously¹ for Fe-doped devices, the I-V characteristics are strongly influenced by the uniformity of the illumination pattern between the electrodes. This effect is illustrated in Figure 1-3, which shows the I-V characteristics of simple-gap-geometry (see top of Figure 1-1) Ti- and Fe-doped devices observed when a laser beam is focused at different positions between the electrodes. When the beam is centered, the I-V curves show the same antisymmetrical character observed with uniform illumination. Note, in contrast to the low-bias region, the photocurrent is about five times higher for the Fe-doped device than for the Ti-doped device at a bias of 3 V. We believe the increasing photocurrent above the knee is due to electron injection at the nonohmic contacts. The differences in the shape of the I-V curves for the Ti- and Fe-doped devices probably are related to subtle differences in the contact barriers and the different type of deep levels (acceptors in the case of Fe and donors in the case of Ti) near these barriers. With ohmic contacts, the I-V characteristics should be linear up to a maximum photoconductive gain of ≈ 15 , which is the electron-to-hole mobility ratio for SI InP. However, with contact barriers, holes tend to accumulate near the cathode and deep levels are expected to play an important role in the recombination process. At room temperature, the Ti-doped material has a high density of un-ionized deep donor levels, which can capture photogenerated holes and provide an increased probability of recombination at the cathode. However, the photogenerated holes in Fe-doped material remain in the valence band and encounter a large barrier at the cathode, which is expected to give rise to large space-charge effects. Photogenerated electrons in

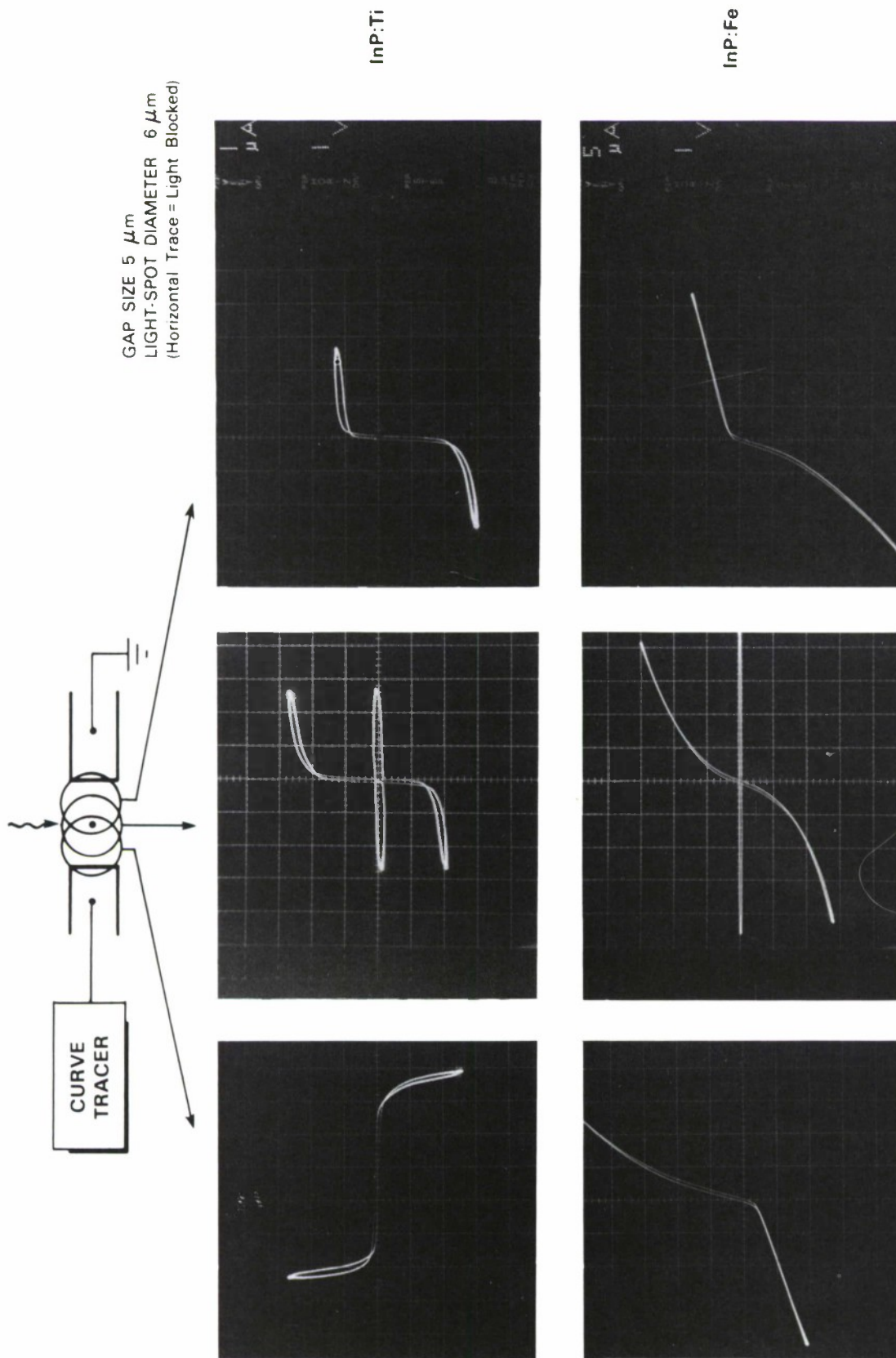


Figure 1-3. Effect on I-V characteristics of position of laser spot between electrodes. Hysteresis is due to curve tracer. Notice different vertical scales for the two series.

Fe-doped material can drop to the acceptor levels and possibly drift to the anode via a hopping mechanism, giving rise to a lower effective mobility and a higher probability of recombination. At very high biases ($\gtrsim 10$ V), carrier avalanche effects also are expected to contribute to the photocurrent, particularly since the electric field distribution between the electrodes is not uniform.

When the beam is moved off center, we find in all cases that the photocurrent increases when moved towards the anode and decreases when moved towards the cathode. A possible explanation for the higher photocurrent observed when illumination takes place close to the positive contact is that the high electric field near the dark cathode reduces the probability of photoelectron recombination before reaching the anode. We have observed this asymmetry in bulk Cr-doped GaAs devices and in GaAs-on-SOS devices. We also found that changing the electrode composition to include a p-type dopant (such as ZnAu) reversed the effect, i.e., the photocurrent increased when the beam was moved towards the cathode.

High-speed photoresponse measurements were carried out using an AlGaAs diode laser driven by a 100-MHz comb generator, with the output of the detector directly fed into a 50-ohm sampling oscilloscope. Figure 1-4 shows the observed responses of Ti- and Fe-doped switches under similar illumination conditions. In order for the signals to exceed sampling scope noise, it was necessary to bias the devices well above the knee of their I-V curves. the Ti-doped switch was biased at 10 V and the bias on the Fe-doped switch was increased to 33 V to produce a similar peak pulse height. the Ti-doped device shows a FWHM (full-width-half-maximum) of 63 ps, which is very close to the 40-ps limit of the test system. The Fe-doped switch shows a much slower (≈ 1 ns) exponential decay. However, the time-integrated signal from the Fe-doped switch is about 20 times that from the Ti-doped switch, which is consistent with the ratio of the dc response of the switches at these high bias levels.

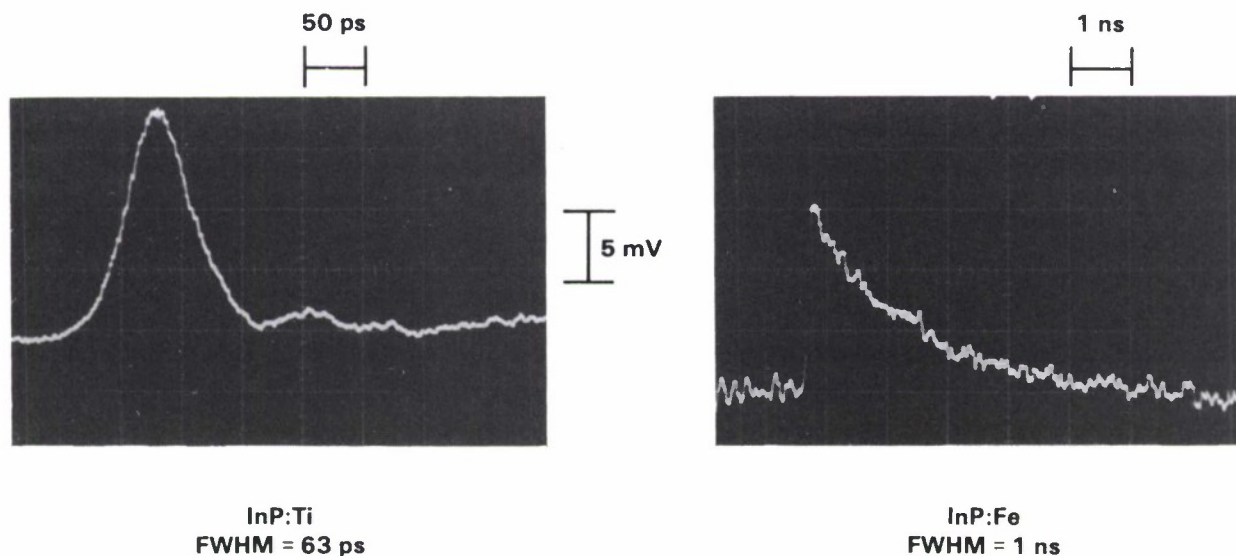


Figure 1-4. Response of Ti- and Fe-doped InP switches to a 40-ps optical pulse.

An interesting application for the optoelectronic switch is in a sample-and-hold circuit,² in which an electrical input signal is sampled by an optical pulse train. For this application, the switch must be in the high-conductance state only during illumination. To check device performance, we used a square wave to simulate the electrical input and a pulsed diode laser to provide the optical input. A scope was used to monitor the inputs and the switch output under illumination and in the dark. A schematic of the waveforms and reference conditions is shown (not to scale) in Figure 1-5. The optical pulses are expected to cause a small electrical output

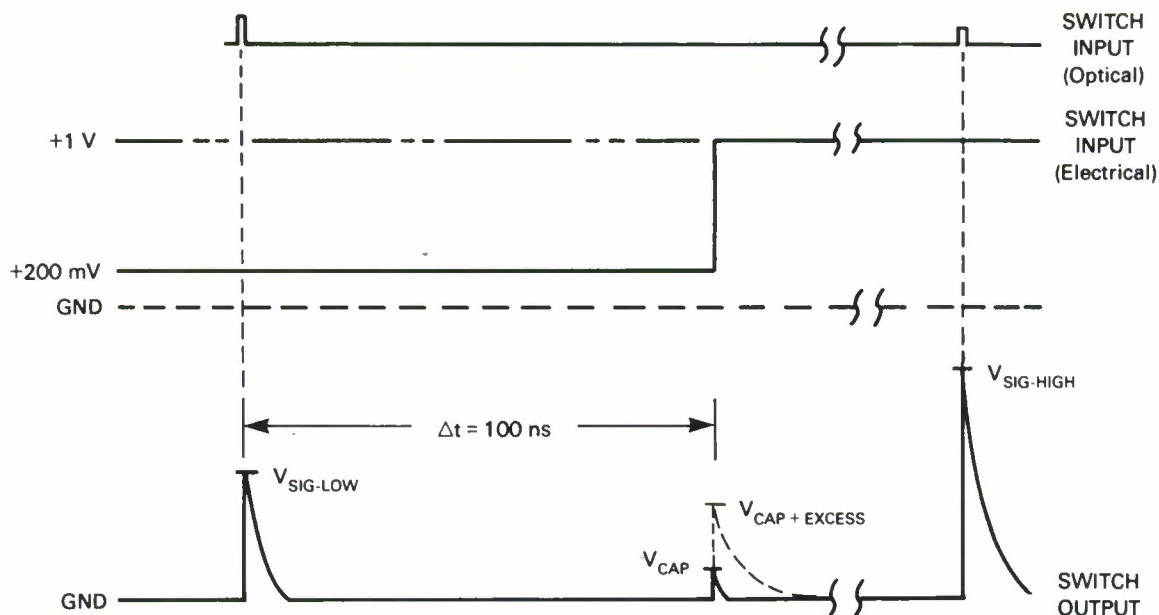


Figure 1-5. Waveforms and reference conditions for step-bias measurements and expected switch response (not to scale).

pulse from the switch during the low-voltage (0.2 V) part of the square wave and a higher signal during the high-voltage (1 V) part. In addition, some capacitive feedthrough should occur at the time of the voltage step. Of concern has been the 'excess' feedthrough at the voltage step, as shown by the dashed line in the switch output.² Experimental results for Fe- and Ti-doped switches are shown in Figure 1-6. From top to bottom are the scope traces for the electrical input to the switch (bias), the optical pulse train (monitored independently), the switch output under illumination (where the high-signal pulse is off the screen) and the output in the dark. A comparison of the two output traces for the Fe-doped switch reveals an excess feedthrough that is considerably larger than the capacitive feedthrough. In contrast, the Ti-doped switch shows little excess feedthrough, as least fifty times less charge than for the Fe-doped switch. The effect appears to be due to the release of charge stored during illumination. The excess feedthrough was found to vary considerably from switch to switch for both Fe- and Ti-doped devices, but even in

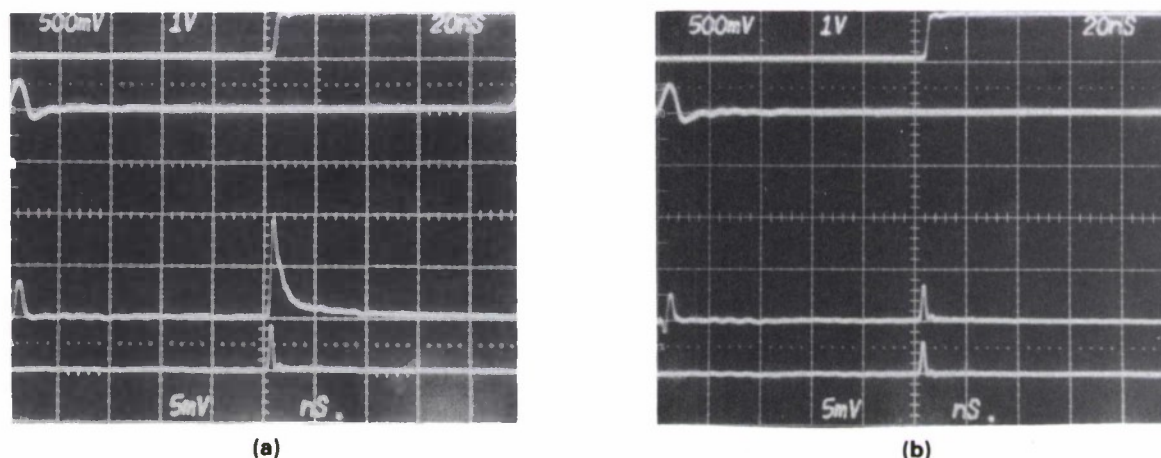


Figure 1-6. Response to optical pulse and step-bias for (a) Fe-doped, and (b) Ti-doped InP switches. Top to bottom are electrical bias, optical input pulse, switch output under illumination, and switch output in the dark (showing capacitive feedthrough.)

the best case the Fe-doped switch had about an order of magnitude more feedthrough than the worst Ti-doped switches. Switches made on a second type of Ti-doped InP, co-doped with S to increase the resistivity, exhibited equally fast response, but had excess feedthrough similar to the Fe-doped switches.

V. Diadiuk	C.H. Cox, III
G.W. Iseler	D.L. Spears
G.A. Ferrante	

1.2 DIODE LASERS WITH CYLINDRICAL MIRROR FACETS

We report the fabrication of diode laser mirrors that are cylindrical, i.e., circularly curved, in the junction plane. The curvature is designed to provide good reflective feedback and simultaneously to form an output lens that reduces the divergence of the output laser beam. These lasers are buried heterostructure (BH) devices fabricated in GaInAsP/InP wafers grown by liquid phase epitaxy and emitting at wavelengths near $1.3 \mu\text{m}$.

The fabrication of the cylindrical facets involved the use of selective chemical etching followed by a mass-transport technique⁴⁻⁷ that was used to smooth the etched surfaces to obtain high optical quality. The overall fabrication of the lasers was identical to that previously described⁷ for two-dimensional arrays of BH lasers with monolithic 45° beam deflectors, except that beam deflectors were omitted and the mirror facets were formed differently. Each laser had a conventional cleaved-facet mirror at one end, and the mirror at the other end of the laser cavity was formed as a circular arc within the plane of the wafer.

As shown from a top view in Figure 1-7, the laser cavity consists of a straight BH waveguide and a fan-shaped end region where the cylindrical mirror facet is formed. The center of curvature of cylindrical facet is at the end of the approximately 2- μm -wide BH waveguide region. Thus, light diffracting out from the end of the BH waveguide expands into the lens

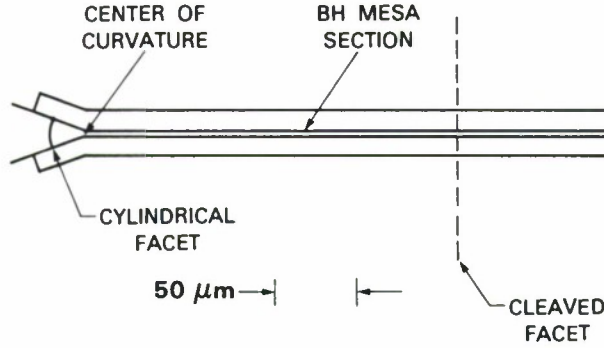


Figure 1-7. Schematic top view of wafer showing a cylindrical mirror facet and a typical cleavage plane that, at opposite ends of the BH mesa section, form the laser cavity.

region and is partially reflected from the circular mirror and imaged back at the end of the waveguide.⁸ The partially transmitted light becomes the output beam. The fan-shaped end region acts as a cylindrical lens and decreases the beam divergence in the plane of the junction. Simple lens equations show that, for the case described here (a source in a plane extending through the center of curvature of a cylindrical lens), there is lateral optical magnification of the BH waveguide termination (as seen looking into the curved output facet) by a factor equal to the index n_g of the lens medium.

Because the effective dimension of the radiating source is magnified, a narrower beam in the far field is obtained. For convenience, we define an effective full width of the BH waveguide aperture w_{eff} such that (assuming Gaussian beams)

$$\sin \theta_f = 1.18 \lambda / (\pi w_{\text{eff}}) \quad , \quad (1)$$

where λ is the optical wavelength and θ_f is the angular half-width of the lateral output beam for a conventional flat-mirror facet. Because of the magnification n_g for the cylindrical facets, the angular half-width in the lateral direction θ_c becomes

$$\sin \theta_c = 1.18 \lambda / (\pi n_g w_{\text{eff}}) \quad . \quad (2)$$

From (1) and (2), we see that the cylindrical facet should emit a radiation pattern which is narrower in the lateral direction compared to a flat mirror by approximately a factor of n_g .

Figures 1-8 and 1-9 are experimental radiation patterns from two lasers. Both lasers have a cylindrical facet on one end and a conventional cleaved facet on the other. Radiation patterns from each end are superimposed in the figures. The radiation pattern from the cleaved end is

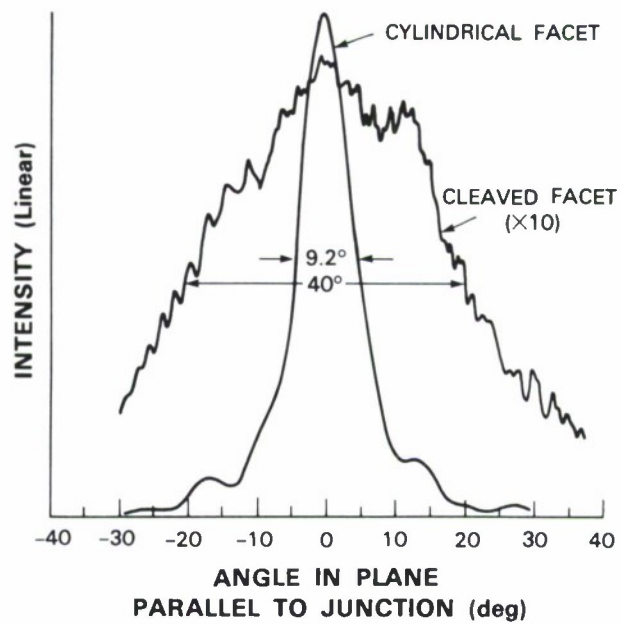


Figure 1-8. Radiation patterns obtained from each end of a laser operating in the lowest-order lateral mode. The FWHM angles are 9.2° and 40° for the cylindrical and cleaved facets, respectively.

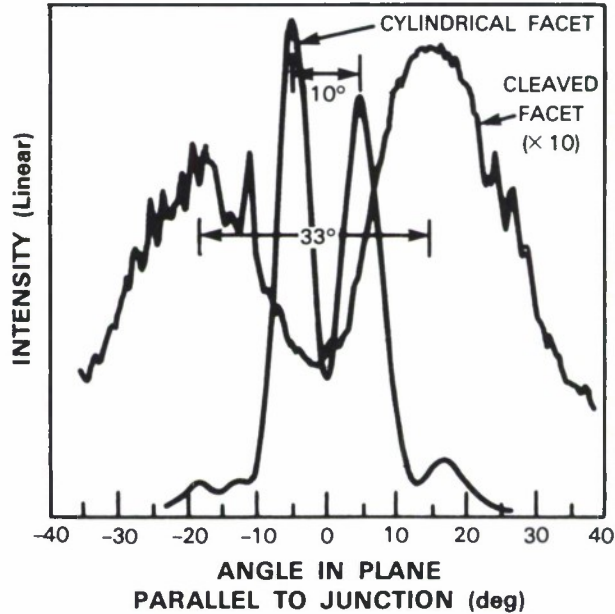


Figure 1-9. Radiation patterns obtained from each end of a laser operating in a second-order lateral mode. The angles between the dominant lobes are indicated.

plotted with an order-of-magnitude greater sensitivity than that from the cylindrical facet. The lower intensity from the cleaved ends results, in part, from the larger angular spread of the radiation patterns in the lateral direction, as predicted. However, the geometry of the lasers also causes a difference in the beam pattern in the transverse direction. This difference can be explained as follows. The lasers had to be saw cut near the cylindrical facet ends to separate the lasers for testing. Since the depth of the etched region in front of the etched cylindrical facets is less than $6\text{ }\mu\text{m}$, it was not possible to avoid leaving a reflecting plane parallel to the junction extending forward from the bottom of the etched cylindrical facets. This plane intercepts some of the output beam in the transverse direction, reflects it, and hence creates a strong ‘double-slit’ interference pattern. Since the lateral radiation pattern was measured in a plane of constructive interference in the transverse pattern, the measured intensity is artificially enhanced relative to that which would have been obtained if the radiation diffracted transversely without being partially intercepted by the reflecting plane. It also should be noted that the rapid variations in intensity with angle seen in the data from the cleaved ends are not noise due to weak signals. These variations are real and reproducible and likely result from scattering of light from the BH sidewalls. Such structure is commonly seen in far-field patterns of BH lasers.

In Figure 1-8, the radiation patterns are consistent with laser oscillation in the lowest order transverse mode. The patterns shown are stable from near threshold (25 mA) to 120 mA. The FWHM spread of the beam from the cylindrical facet end is about 9.2° compared to about 40° from the cleaved end. This difference is somewhat larger than predicted by (1) and (2). We estimate $n_g \simeq 3.4$ for a double heterostructure wafer with an active layer thickness $d \simeq 0.34\text{ }\mu\text{m}$. Using $\theta_c = 9.2^\circ/2$ in (2), we obtain

$$w_{\text{eff}} = 1.785\text{ }\mu\text{m} \quad . \quad (3)$$

This value of w_{eff} when used in (1) yields a FWHM angle of

$$2\theta_f = 30.6^\circ \quad . \quad (4)$$

There are several possible reasons for the discrepancy. The radiation pattern from the cleaved end may be artificially broadened by the scattered light mentioned above. In addition, the somewhat ragged pattern makes it difficult to measure and define an effective half width clearly. It is also possible that the lens curvature can be distorted during fabrication, which can lead to a larger lens magnification at the expense of less mirror feedback.

Figure 1.9 shows the radiation patterns from a device that appears to be operating in the next higher lateral mode. In this case, we can compare the angular separations between the pairs of peaks. We obtain 10° from the cylindrical facet end and about 33° from the cleaved end in close agreement with the expected factor of $n_g \simeq 3.4$.

In summary, we have demonstrated low threshold current lasers (as low as 25 mA) having one mirror circularly curved in the junction plane to provide optical feedback as well as a lens effect. These lasers are useful to improve coupling into optical fibers. The design also can be used

in two-dimensional arrays with 45° beam deflectors and in Y-coupled linear arrays⁹ to improve the output beam quality.

J.N. Walpole	L.J. Missaggia
Z-L. Liao	D. Yap

REFERENCES

1. Solid State Research Report, Lincoln Laboratory, MIT (1984:2), p. 11, DTIC AD-A147640.
2. Solid State Research Report, Lincoln Laboratory, MIT (1984:3), p. 85, DTIC AD-A154783.
3. G.W. Iseler and B.S. Ahern, Appl. Phys. Lett. **48**, 1656 (1986).
4. Z-L. Liao and J.N. Walpole, Appl. Phys. Lett. **40**, 568 (1982).
5. Z-L. Liao and J.N. Walpole, and D.Z. Tsang, Appl. Phys. Lett. **44**, 945 (1984).
6. Z-L. Liao and J.N. Walpole, Appl. Phys. Lett. **46**, 115 (1985).
7. J.N. Walpole and Z-L. Liao, Appl. Phys. Lett. **48**, 1636 (1986).
8. The image is inverted after reflection, but coupling should be large, since the waveguide is symmetric.
9. D.F. Welch, P.S. Cross, D. Scifres, W. Streifer, and R.D. Burnham, Electron. Lett. **22**, 293 (1986).

2. QUANTUM ELECTRONICS

2.1 Ti:Al₂O₃ LASER DEVELOPMENT

We recently reported¹ the room-temperature CW operation of a Ti:Al₂O₃ laser pumped with an argon-ion laser. Using the same laser rod, which contains about 0.02 wt.% Ti₂O₃, we now have achieved CW operation at temperatures up to 120°C. Figure 2-1 shows the threshold pump

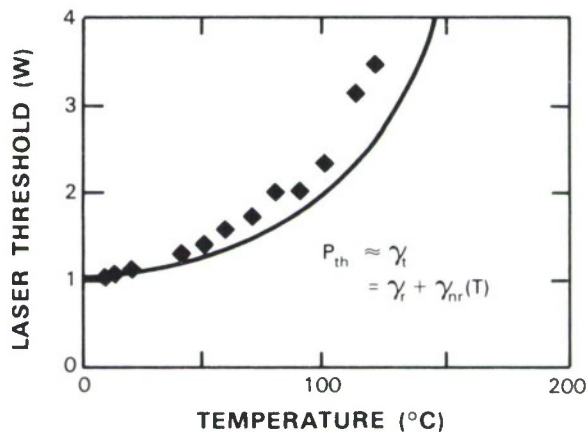
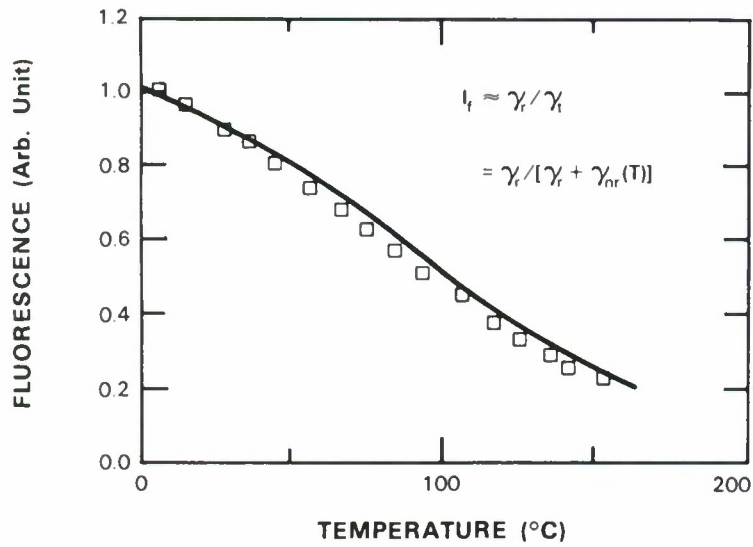


Figure 2-1. Threshold pump power P_{th} for a Ti:Al₂O₃ laser as a function of temperature. The circles represent the data points and the curve represents the predicted variation based on the known temperature dependence of the total relaxation rate, γ_t .

power P_{th} for laser emission at ~ 780 nm as a function of heat sink temperature. The experimental points are compared with a normalized curve that was calculated from the relationship $P_{th} \propto \gamma_t$, where γ_t is the total relaxation rate for spontaneous fluorescence, by using the published data^{2,3} for the temperature dependence of γ_t . It is believed that the deviations observed at higher temperatures occur because the temperature of the lasing filament becomes greater than the measured heat sink temperature.

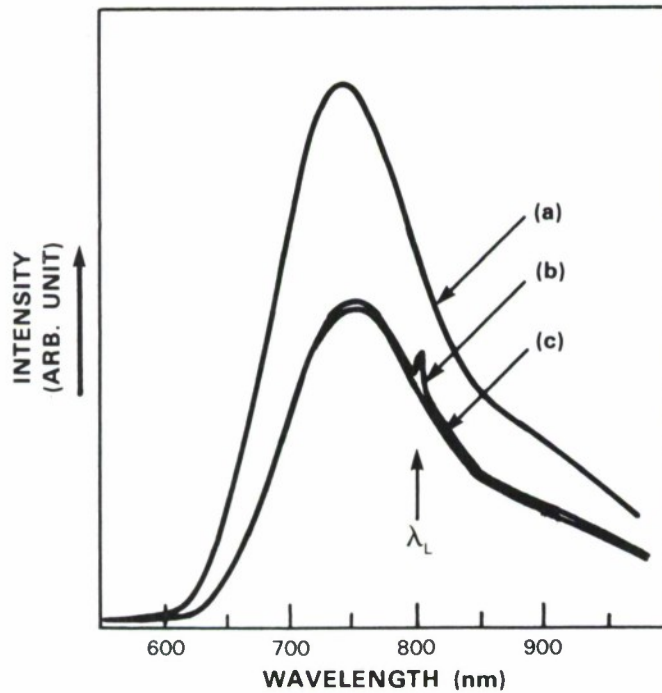
The intensity I_f of the spontaneous fluorescence emitted by the laser rod at a fixed pump power below threshold is plotted against temperature in Figure 2-2. The experimental points are fit well by the normalized curve shown, which was calculated from the relationship $I_f \propto \gamma_r/\gamma_t$, where γ_r is the radiative relaxation rate, by again using the published data^{2,3} for the temperature dependence of γ_t and also making the assumption that γ_r is independent of temperature. The good fit verifies this assumption. Since $\gamma_t = \gamma_r + \gamma_{nr}$, where γ_{nr} is the nonradiative relaxation rate, it can be concluded that the increase in γ_t and P_{th} with temperature is due entirely to the increase in γ_{nr} .

It generally has been assumed that the fluorescence responsible for Ti:Al₂O₃ laser action is broadened homogeneously. We have verified this assumption by measuring the spectral



76401-9

Figure 2-2. Spontaneous fluorescence intensity for a Ti:Al₂O₃ laser as a function of temperature. The circles represent the data points and the curve represents the predicted variation assuming that only the nonradiative relaxation rate γ_{nr} is temperature dependent.



76401-10

Figure 2-3. Spontaneous fluorescence spectra for the Ti:Al₂O₃ laser recorded when the laser is (a) off, (b) on, and (c) at threshold. The spike at λ_L is due to scattered radiation from the laser.

distribution of the spontaneous fluorescence emitted by the laser rod in a direction perpendicular to the axis of the rod. The results are shown in Figure 2-3, where the spectra obtained for three different operating conditions are plotted on the same intensity scale. Trace (a) is the spectrum obtained when the pump power was about 1-8 times the threshold value but laser action was prevented by inserting an absorber in the laser cavity. When the absorber was removed, laser action took place at $\lambda_L \sim 800$ nm, and the fluorescence intensity was reduced by the same factor at all wavelengths, as shown by trace (b). (The small spike at λ_L results from scattering of the laser radiation.) The uniform decrease in intensity establishes that the Ti:Al₂O₃ transition is homogeneously broadened. Trace (c) is the fluorescence spectrum obtained when the pump power was decreased to the threshold value. As expected, this trace is almost coincident with trace (b).

In addition to the laser rod used in the above experiments, we have fabricated five new Ti:Al₂O₃ rods containing up to 0.1 wt.% Ti₂O₃. Room-temperature CW laser action has been obtained for all five. The laser data have been analyzed to determine the residual infrared absorption at λ_L . The results are generally consistent with those obtained from spectrometer measurements, which show that the residual absorption increases quadratically with Ti³⁺ concentration.⁴

A. Sanchez R.E. Fahey
R.L. Aggarwal A.J. Strauss

2.2 ELECTRO-OPTIC TUNING OF A Ti:Al₂O₃ LASER

An electro-optic birefringent element based on the design shown in Figure 2-4 has been fabricated, using a LiNbO₃ crystal that had been antireflection (AR) coated on the end faces for 775 nm. This device has been used for intracavity tuning experiments on an Ar laser-pumped

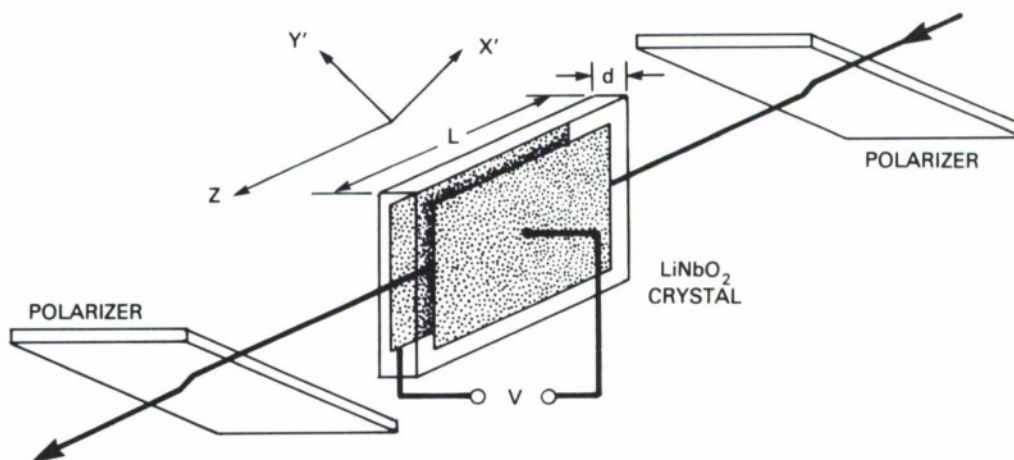


Figure 2-4. Principle of operation of the electro-optic filter. For the device described in the text, $d = 1$ mm, $L = 25$ mm.

Ti:Al₂O₃ laser. The first issue was that of optical damage (photorefractive effect): because of published data on the temperature dependence of optical damage in LiNbO₃,⁵ provision was made to heat the crystal up to 200°C. After several experiments, it was determined that a large photorefractive effect was due to the residual pump light (at 488 and 514.5 nm) entering the LiNbO₃ crystal; while operation at high temperature reduced the effect to the point where lasing became possible, this was only true with no voltage applied across the crystal. Attempts at using the crystal for its intended electro-optic function failed, as lasing would stop within a few seconds of turning the voltage on. The problem was solved by separating the (green) pump and (infrared) laser beams with two prisms, as shown in Figure 2-5; the prism refractive index and angle insure incidence at close to Brewster's angle with low reflection losses. The beam separation provided is ample, several millimeters.

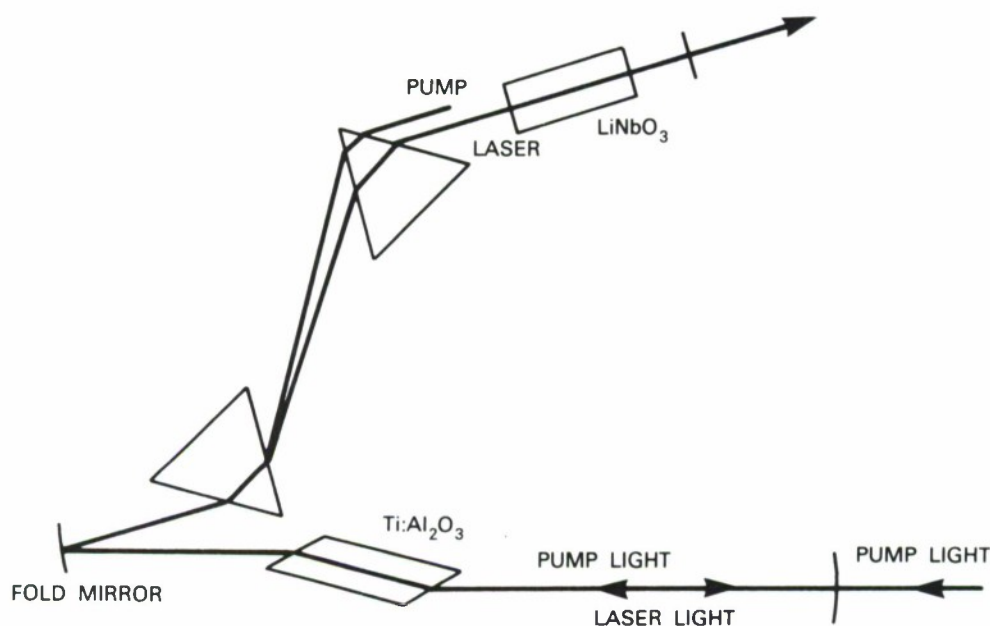


Figure 2-5. Cavity layout of the electro-optically tuned Ti:Al₂O₃ laser.

With the arrangement of Figure 2-5, optical damage is nearly undetectable across the Ti:Al₂O₃ tuning range, and electro-optic tuning is possible as expected for a 1-stage birefringent filter; static tuning over several orders is shown in Figure 2-6. The tuning range observed is limited at the short-wavelength end by reflection losses from the LiNbO₃ crystal faces; it should be possible to reduce these by optimization of the AR coating or operation at Brewster's angle. The LiNbO₃ device operates satisfactorily at room temperature; in fact, raising the temperature seems to induce extra losses (increased lasing threshold) for high applied voltages. The only

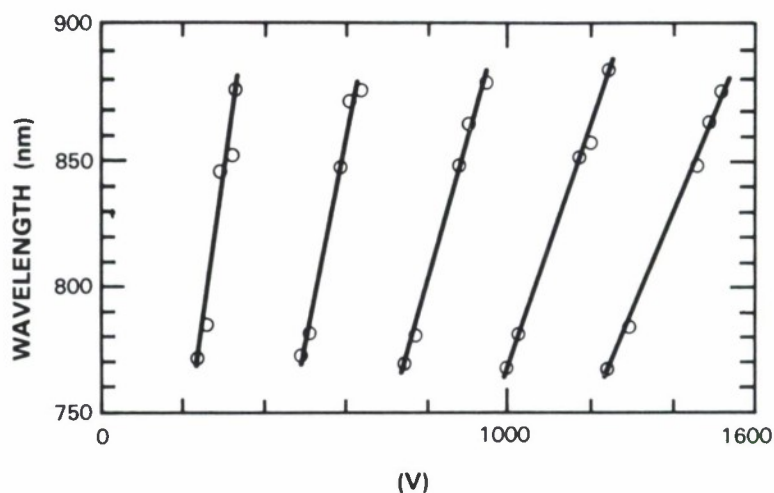


Figure 2-6. Static tuning curves of the $\text{Ti:Al}_2\text{O}_3$ laser.

drawback, possibly related to a small residual photorefractive effect, is a slight hysteresis (shifting of the tuning curves) after operation at high voltages for several hours; this should be of little consequence for the final device, where the controlling voltages will be driven by a feedback system.

V. Daneu

2.3 Er:YAG LASER DEVELOPMENT

An investigation has been made of the temperature dependence and pumping threshold for CW operation of the $1.65\text{-}\mu\text{m}$ Er:YAG laser using a $1.47\text{-}\mu\text{m}$ laser as an optical pump. The laser cavity was as reported previously,⁶ with the addition that the temperature of the Er:YAG crystal was controlled and monitored over the temperature range of 77 K to 300 K. With a maximum pump intensity of 150 W/cm^2 , laser operation was successful only over the temperature range of 77 K to approximately 190 K, with most of the decrease in laser operation occurring between 160 K and 190 K; no laser operation was observed at 195 K or 300 K. The laser threshold at 77 K was approximately 40 W/cm^2 . Previous calculations had indicated that lasing should have been observed at temperatures up to 300 K, and, in addition, the threshold for 77 K should have been much lower, on the order of 2 W/cm^2 .

Some preliminary work has been conducted to understand the above discrepancy between experiment and calculation. Other work⁷ has shown that parasitic phonon-assisted upconversion may be an important process in the exchange of excitation between Er ions. The incorporation of such a process to the energy levels involved in the Er:YAG laser is shown in Figure 2-7. In order better to understand this process and determine whether or not it has any influence on the observed decrease in Er:YAG laser operation, several preliminary experiments have been

conducted. These include the measurement of the fluorescence decay time of the $I_{13/2}$ level ($1.65 \mu\text{m}$) immediately after pulsed excitation at $1.47 \mu\text{m}$; the results indicate that the upconversion process increased the decay rate relative to the normal rate by as much as a factor of 5. Preliminary measurements of the temporal shape of the fluorescence intensity from the $I_{13/2}$ level as a function of excitation intensity also are consistent with the parasitic process shown in Figure 2-7.

D.K. Killinger

2.4 LASER FREQUENCY CONVERSION

A study has continued of the feasibility of using frequency conversion in nonlinear crystals to achieve efficiently a high-energy, high-average-power output at ~ 550 nm by tripling $1.65\text{-}\mu\text{m}$ pulsed laser radiation as well as to achieve similar output at 530 nm by frequency doubling the Nd:YAG laser radiation.

A. $1.65\text{-}\mu\text{m}$ Conversion

The only available source of coherent radiation at $1.65\text{ }\mu\text{m}$ is a continuously tunable Co:MgF_2 laser. The laser was operated in a pulsed, Q-switched mode. Under these conditions, the laser produced ~ 7 to 10 mJ per pulse in a TEM_{00} mode with a pulse length $\tau \sim 1\text{ }\mu\text{s}$. The laser output was used to investigate second harmonic generation (SHG) and damage threshold properties of KTP and LiIO_3 crystals, using the experimental arrangement shown in Figure 2-8.

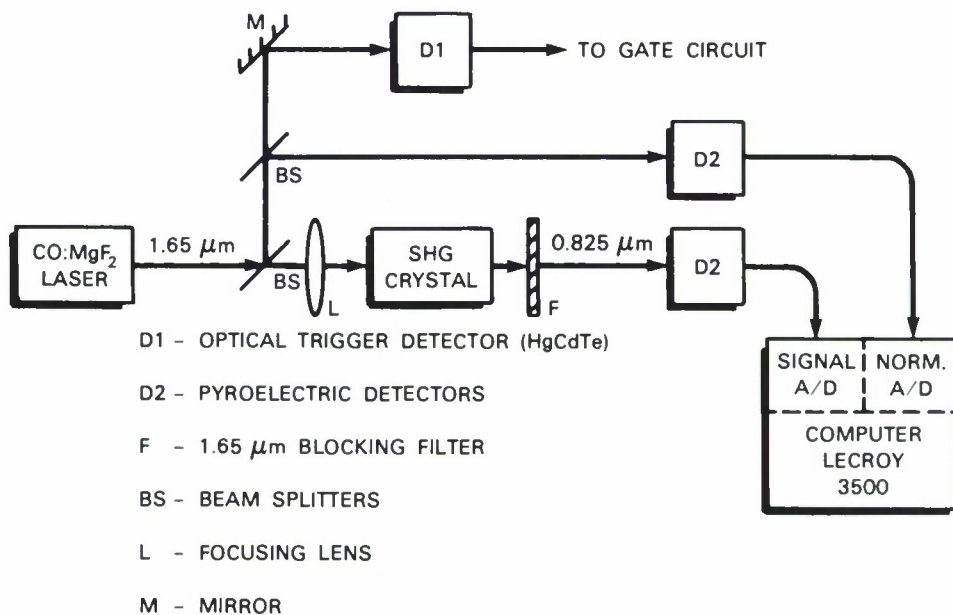


Figure 2-8. Experimental arrangement for second harmonic generation at $1.65\text{ }\mu\text{m}$.

The limited pulse energy available necessitated strong focusing to obtain high power densities within the SHG crystals. The lenses used for this purpose ranged in focal lengths from 1.5 to 50 cm.

For SHG at $1.65\text{ }\mu\text{m}$, both LiIO_3 and KTP have small phase-matching acceptance angles (FWHM = 1.3 and 1.7 mrad-cm, respectively) and large walk-off angles (3.2° and 2.4° , respectively). Therefore, significant SHG slope efficiency values were obtainable only with the

longest focal length lens. With this lens, initial SHG efficiency slopes of 0.07% and 0.14% $\text{MW}^{-1}\text{cm}^2$ were obtained for 5-mm-length LiIO_3 and KTP samples; these correspond to one-half and one-eighth the expected values, respectively. The predicted value for KTP is based on an early literature value; however, the much lower value presently observed is consistent with other recent reports. X-rays of our KTP samples have shown the existence of twinning within the crystals. We believe this to be a major factor in reducing the efficiency of KTP frequency conversion.

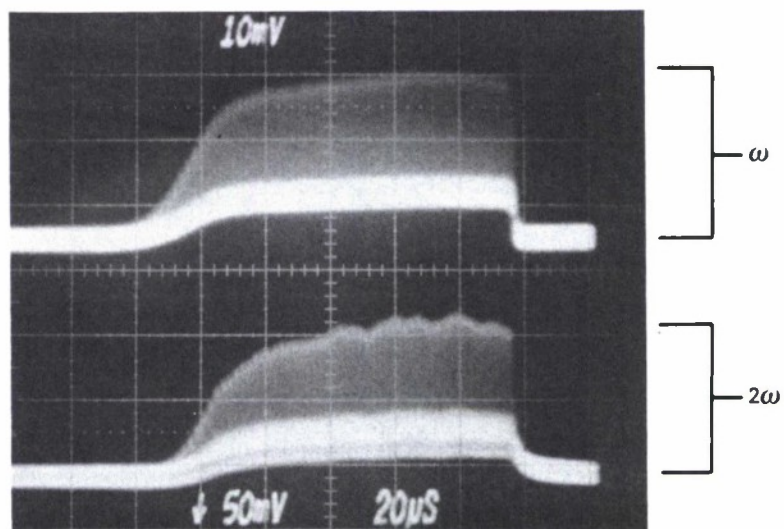
The shorter focal length lenses were used to increase the power density to the crystals in order to determine their damage threshold. With the laser operating at a 2-Hz PRF, a 3-mm-long KTP crystal sustained damage at 80 MW/cm^2 , and the 5-mm-long KTP crystal was damaged at 100 MW/cm^2 . In both cases, crater-like damage was observed at the input face of the crystal and occurred after operating with no visible damage for approximately 100 pulses. Damage thresholds varying between 150 and 650 MW/cm^2 previously have been reported for KTP when irradiated by Q-switched 30-ns Nd:YAG laser pulses.⁸ The LiIO_3 crystal remained undamaged after irradiation with a laser pulse density exceeding 550 MW/cm^2 . The low SHG efficiency slope of KTP, coupled with a damage threshold below 100 MW/cm^2 for a $1\text{-}\mu\text{s}$ pulse length, appears to eliminate this material, in its present state of crystal growth development, from consideration for conversion from $1.65 \mu\text{m}$.

LiIO_3 has a generally poor SHG efficiency slope, but in view of its surprisingly high damage threshold at $1.65 \mu\text{m}$, it cannot be eliminated as a possible candidate for the first stage (doubling) of the frequency tripling process. To be a viable candidate, the damage threshold of LiIO_3 must remain high while serving as an efficient frequency doubler to 825 nm. Whether it meets this further requirement can be established only when a $1.65 \mu\text{m}$ source capable of producing a collimated beam at the necessary power density becomes available.

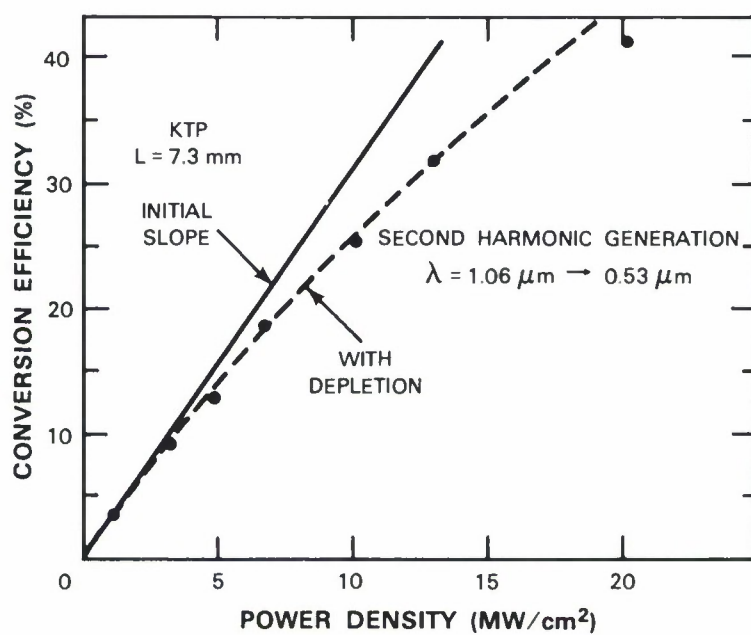
B. 1.06- μm Conversion

A Nd:YAG laser system has been received that is capable of producing mode-locked pulses of 50- to $200\text{-}\mu\text{s}$ length with 2 to 3 joules per pulse outputs at PRFs up to 10 Hz. It is being used to study SHG effects in KTP. An initial experiment carried out with this laser used a $100\text{-}\mu\text{s}$ -duration pulse, as shown in Figure 2-9(a), having a pulse energy of 640 mJ and a 1-Hz repetition rate. The frequency doubler was an antireflection coated KTP crystal $3 \text{ mm} \times 3 \text{ mm} \times 7.3 \text{ mm}$ long. The doubled output also is shown in Figure 2-9(a). The conversion efficiency as a function of input power density is given in Figure 2-9(b). For a damage threshold⁹ near 50 MW/cm^2 , efficiencies well in excess of 50% should be achievable.

N. Menyuk
K.F. Wall
W.E. DeFeo



(a)



(b)

Figure 2-9. (a) Simultaneous oscilloscope traces of laser input to KTP crystal at fundamental frequency ω and second harmonic 2ω , (b) second harmonic efficiency as a function of laser input power density.

REFERENCES

1. A. Sanchez, R.E. Fahey, A.J. Strauss, and R.L. Aggarwal, *Opt. Lett.* **11**, 363 (1986).
2. P.F. Moulton, *J. Opt. Soc. Am. B* **3**, 125 (1986).
3. P. Albers, E. Stark, and G. Huber, *J. Opt. Soc. Am. B* **3**, 134 (1986).
4. Solid State Research Report, Lincoln Laboratory, MIT (1986:2), p. 9.
5. A. Ashkin, G.D. Boyd, J.M. Dziedzic, R.G. Smith, A.A. Ballman, J.J. Levinstein, and K. Nassau, *Appl. Phys. Lett.* **9**, 72 (1966).
6. Solid State Research Report, Lincoln Laboratory, MIT (1986:2), p. 10.
7. V.I. Zhekov, T.M. Murina, A.M. Prokhorov, M.I. Studenikin, S. Georgescu, J. Lupei, and I. Ursu, *Sov. J. Quantum Electron.* **16**, 274 (1986).
8. T.A. Driscoll, H.J. Hoffman, R.E. Stone and P.E. Perkins, *J. Opt. Soc. Am. B* **3**, 683 (1986).
9. S.E. Moody, J.M. Eggleston, III, and J. Seamans, *Tech. Digest CLEO*, 258 (1986).

3. MATERIALS RESEARCH

3.1 TRACER GAS STUDIES FOR OMVPE REACTOR DESIGN

To obtain data for optimizing the design and operation of reactors for the growth of III-V layers by organometallic vapor phase epitaxy (OMVPE), we recently carried out an investigation in which the gas flow patterns in a vertical reactor tube with a disk susceptor were visualized by using a sheet of laser light to illuminate smoke particles of TiO_2 transported through the tube in a stream of He gas.¹ It was found that uniform, laminar flow without vortex formation can be achieved under isothermal conditions by injecting the gas into the tube through a porous plug, and that convective instabilities due to heating the susceptor or to successively introducing gases of different densities can be minimized by operation at reduced pressure.

To produce the multilayer structures needed for electronic and optoelectronic applications, the composition of the gas mixture reaching the heated substrate is varied by making stepwise changes in the rates at which the different reactant gases are injected into the carrier gas stream. Many of these applications require abrupt interfaces between the successive epilayers. Uniform, vortex-free flow within the reactor tube is not sufficient to insure such interfaces because, as the gas mixture traverses the tube, the boundaries between adjacent regions with different compositions tend to become less abrupt as a result of gaseous diffusion or of convection arising from radial variations in the gas velocity parallel to the axis of the tube. To investigate these dispersive effects, we have performed tracer gas experiments in which the concentration of gaseous SF_6 just above the susceptor disk was measured as a function of time after the flow of SF_6 into the He stream was switched on or off. The rate of change in this concentration should be correlated with the abruptness of the interfaces between successive epitaxial layers. These experiments employed a fast-switching, pressure-balanced manifold for introducing the SF_6 . The gas mixture was injected into the reactor tube at atmospheric pressure through a porous plug, and the susceptor was not heated.

In one series of experiments, the flow of SF_6 was switched on at time $t = 0$, producing a concentration C_0 in the incoming gas stream, and switched off at $t = 60$ s. In Figure 3-1, the ratio C/C_0 , where C is the SF_6 concentration measured at the susceptor, is plotted as a function of time for He flow rates (v) of 2, 5, and 10 lpm, and for distances (L) between the gas inlet and the susceptor of approximately 16 cm [Figure 3-1(a)] and 4 cm [Figure 3-1(b)]. In each case, there is a delay before SF_6 is first detected, because of the time required for the gas to travel through the lines and the reactor tube to the susceptor. The delay time decreases as v increases because the transit time is inversely proportional to v . The delay also decreases as L decreases, indicating that the gas residence time within the portion of the reactor tube above the susceptor (proportional to L/v) is significantly greater than the residence time within the input lines.

After the SF_6 is initially detected, C/C_0 gradually increases to one, rather than increasing abruptly. It can be concluded that the interfaces between epitaxial layers grown under similar conditions would be graded rather than abrupt. The time required for C/C_0 to reach one is a

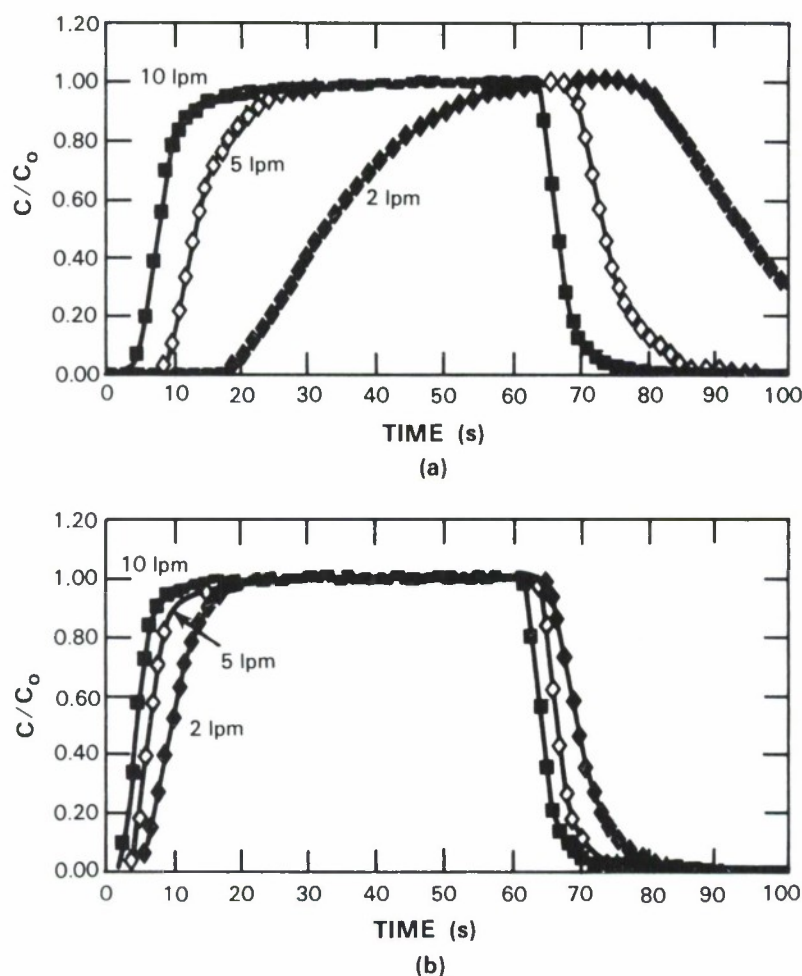


Figure 3-1. Time dependence of C/C_0 , where C is the SF_6 concentration measured at the susceptor of a vertical reactor tube and C_0 is the initial concentration in the gas stream, for SF_6 flow switched on at $t = 0$ and switched off at $t = 60$ s. Inlet-to-susceptor distance: (a) 16 cm, (b) 4 cm.

measure of the degree to which the boundary between the region of pure He and the following region containing SF_6 is smeared out by dispersive effects. This time is found to decrease as v increases and L decreases, as expected because reducing the residence time allows less time for the dispersive effects to occur. (The response time observed at $v = 10$ lpm and $L = 4$ cm appears to be limited by the time constant of the SF_6 measuring system, which is about 1 s.) Except for $v = 2$ lpm and $L = 16$ cm, the lowest flow rate combined with the longer distance, the steady state is achieved well before $t = 60$ s. When the SF_6 flow is switched off, the inverse process occurs, with C/C_0 decreasing to zero. Again, the delay time before C begins to change and the time required to reach the steady state both decrease as v increases and L decreases.

For the growth of superlattice structures, the flows of reactant gases are switched on and off periodically. In a second series of tracer gas experiments, the flow of SF_6 was switched on and off at intervals of 18 s. Figure 3-2 shows the time dependence of C/C_0 obtained for $v = 2, 5$, and 10 lpm and for $L = 16$ and 4 cm. As in Figure 3-1, with increasing v and decreasing L , the rate of change of C/C_0 increases, indicating that the interfaces between successive layers in a superlattice would become more abrupt.

C.A. Wang

3.2 RADIATION EFFECTS ON CMOS CIRCUITS FABRICATED IN SOI FILMS

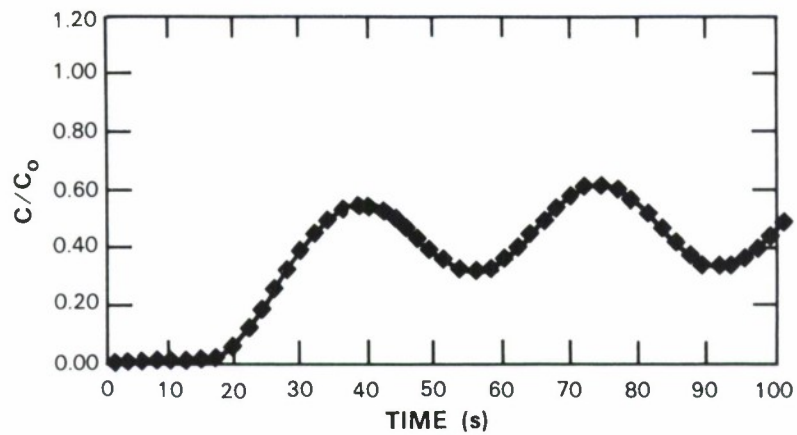
In the program to develop integrated circuit technology utilizing silicon-on-insulator (SOI) films, we previously fabricated² CMOS 1 K static random-access memories (SRAMs) in such films prepared by zone-melting recrystallization (ZMR). We now have fabricated fully functional CMOS 1.2 K gate arrays and 1 K SRAMs in both ZMR and oxygen-ion-implanted (SIMOX) SOI films, and transient and total-dose radiation tests have been performed on these circuits.

The graphite-strip-heater technique³ was used to prepare ZMR SOI wafers consisting of a 0.3- μm -thick Si film and a 1.75- μm -thick buried SiO_2 layer on a Si substrate. Commercial SIMOX SOI wafers, which had been implanted with oxygen at 160 keV to a dose of $2 \times 10^{18} \text{ cm}^{-2}$, were subsequently annealed at 1200°C. The thicknesses of the Si film and buried-oxide layer are 0.15 and 0.3 μm , respectively.

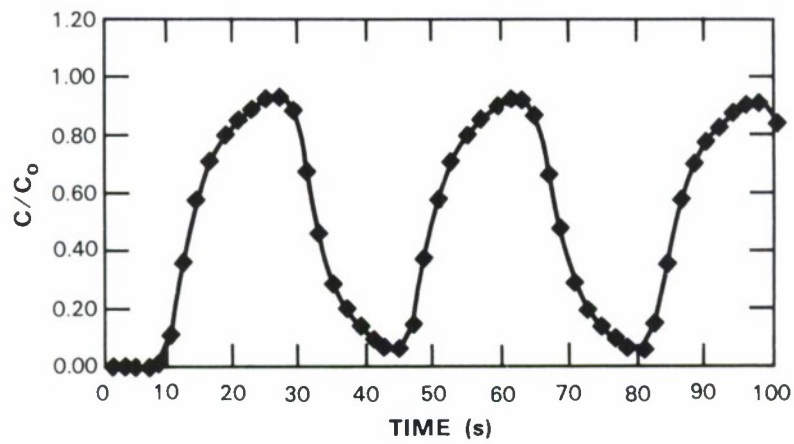
The two types of SOI wafers were processed simultaneously in a single-poly, single-metal CMOS run. Each wafer contains three different circuits: 1.2 K gate array, 1 K SRAM, and Brutus test chip. All three circuits were originally designed for fabrication in SOS wafers. The minimum feature sizes for the gate arrays and SRAMs are 3 and 4 μm , respectively. Figures 3-3 and 3-4 are photographs of a completed gate array and SRAM, which have chip sizes of $\sim 6 \times 6$ and $3.5 \times 5 \text{ mm}$, respectively.

The results of systematic measurements of the test chip transistor characteristics are summarized in Table 3-1. For both n- and p-channel devices, the gate length (L) and width (W) are 3 and 50 μm , respectively, and the gate oxide thickness is 35 nm. The n- and p-channel low-field mobilities for the ZMR devices are comparable to the bulk values, while those for the SIMOX devices are, respectively, 8% and 15% lower. Both leakage current and inverse subthreshold slopes are smaller for the ZMR devices. These results indicate that the ZMR films are superior in crystal quality to the SIMOX films. The uniformity of V_T is better for the SIMOX devices. Furthermore, V_T for the SIMOX devices is insensitive to the bias voltage (V_B) applied to the Si substrate.

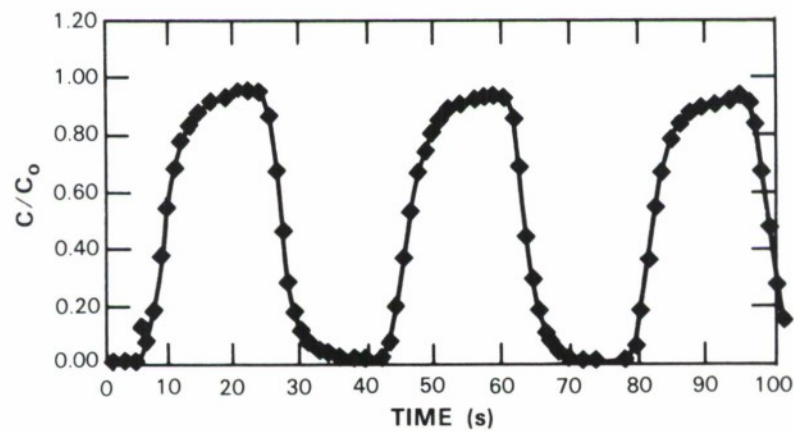
Table 3-2 summarizes the speed performance of various test circuits and the yield of functional gate arrays. All data were obtained at a supply voltage of 5 V and zero substrate bias. The measured propagation delays for 3- μm gate length ring oscillators are 380 and 720 ps, respectively, for the ZMR and SIMOX circuits. The ZMR circuits are faster because their parasitic capacitance is smaller; the capacitance is smaller because the buried-oxide thickness is



(a) 2 lpm



(b) 5 lpm



(c) 10 lpm

Figure 3-2. Time dependence of C/C_0 for SF_6 flow switched on and off at intervals of 18 s. Inlet-to-susceptor distance: (a)–(c) 16 cm, (d)–(f) 4 cm.

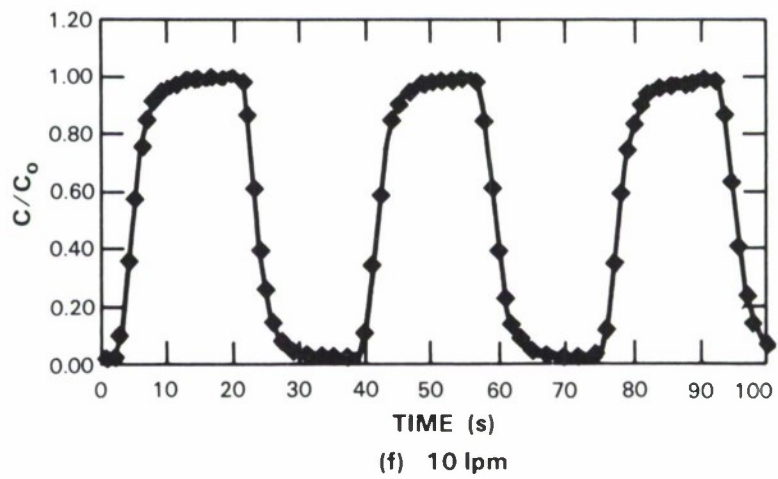
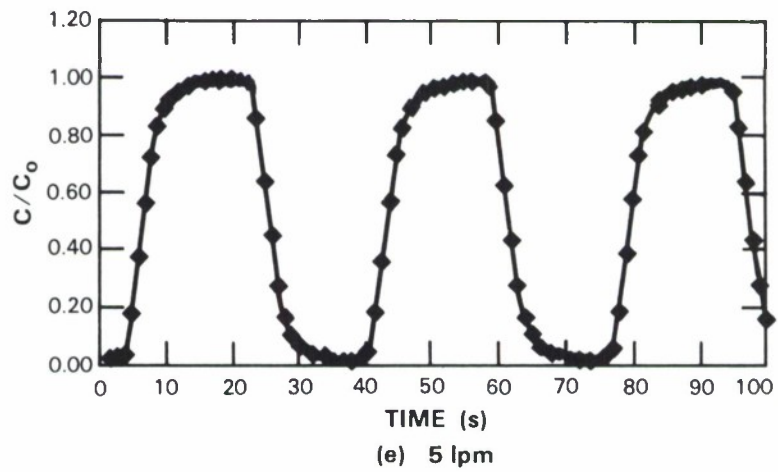
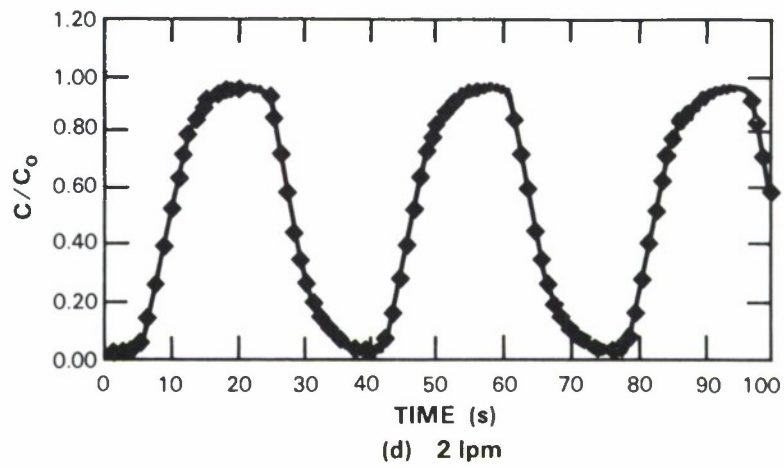


Figure 3-2. Continued.

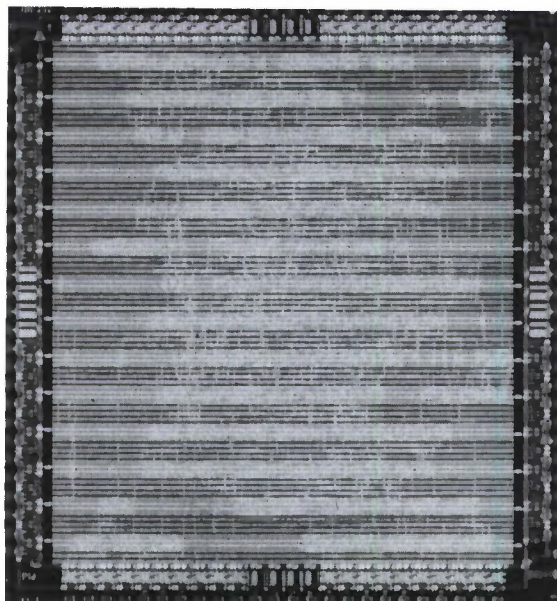


Figure 3-3. Photograph of a 1.2-K SOI/CMOS gate array.

76401-20

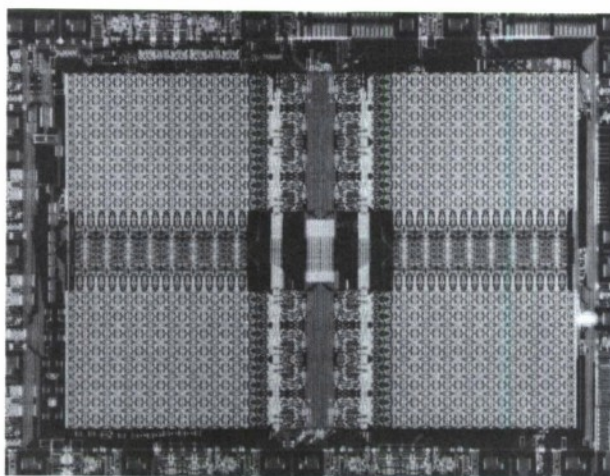


Figure 3-4. Photograph of a 1-K SOI/CMOS SRAM.

76401-21

TABLE 3-1			
Comparison of ZMR and SIMOX CMOS Device Characteristics			
Low Field Mobility	ZMR		SIMOX
	μ_n		$600 \text{ cm}^2/\text{V-s}$
	μ_p		$215 \text{ cm}^2/\text{V-s}$
Leakage Current	$\leq 1 \text{ pA}$		$\sim 10 \text{ pA}$
Inverse Subthreshold Slope	67 mV (n-ch.)		100 mV (n-ch.)
	90 mV (p-ch.)		130 mV (p-ch.)
Threshold Voltage V_T	+0.3 V (n-ch.)		+0.6 V (n-ch.)
	-1.1 V (p-ch.)		-1.3 V (p-ch.)
Threshold Voltage Standard Deviation	39 mV		20 mV
Sensitivity of V_T to Substrate Bias	Low (n-ch.)		Low (n-ch.)
	High (p-ch.)		Low (p-ch.)

TABLE 3-2		
Comparison of ZMR and SIMOX Circuit Performance		
Propagation Delay of 39-Stage Ring Oscillators	ZMR	SIMOX
	380 ps	720 ps
Maximum Operating Frequency of Divide-by-32 Circuits	62 MHz	42 MHz
Access Time of 1 K SRAMs	80 ns	120 ns
Wafer Probe Yield of 1.2 K Gate Arrays	40%	65%

considerably greater for the ZMR wafers ($1.75\ \mu\text{m}$) than for the SIMOX wafers ($0.3\ \mu\text{m}$). Consistent with the ring oscillator results, the ZMR divide-by-32 circuits and SRAMs are also superior in speed performance to the SIMOX circuits. However, the yield of fully functional gate arrays, as determined by wafer-probe testing of about 100 circuits, is higher for SIMOX than for ZMR. In addition, as shown in Table 3-1, the ZMR devices are less uniform than the SIMOX devices. Both the device nonuniformity and smaller yield of the ZMR devices probably result from random macroscopic defects, such as protrusions and voids, that are associated with particulate contamination in SOI sample preparation and ZMR processing. Such defects, which are not inherent in the ZMR process, should be reduced substantially or eliminated by careful process control.

Transient radiation tests, using a flash X-ray source with a pulse width of $\sim 20\ \text{ns}$, have been performed on five ZMR and six SIMOX 1 K SRAMs. No logic upset was detected for any of these circuits at dose rates up to $7 \times 10^{10}\ \text{rad/s}$, the highest value attainable with the present equipment. The substrate bias has no detectable effect on memory upset. In a previous study on SIMOX SRAMs, substrate bias reduced the logic upset threshold from 5×10^{10} to $1.6 \times 10^{10}\ \text{rad/s}$.⁴

Total-dose radiation tests using a 1.5-MeV electron beam or Co-60 γ -ray source have been performed on test devices, gate arrays, and SRAMs. A negative substrate bias of $-10\ \text{V}$ was used during irradiation to suppress n-channel leakage current. Figure 3-5 shows V_T for the test devices as a function of total radiation dose. The gate oxide thicknesses are 35 nm for ZMR and 35 and 25 nm for SIMOX devices. For n-channel devices, because of insufficient channel doping, the V_T values are smaller than the desired value ($\sim +1.0\ \text{V}$) for CMOS circuits. When the devices are biased 'ON' during irradiation, V_T shifts significantly, becoming negative at sufficiently high doses. The shifts are most pronounced for 35-nm SIMOX devices. For p-channel devices, the V_T shifts are comparable for 'ON' and 'OFF' states and again are most pronounced for 35-nm SIMOX devices. The relatively large V_T shifts are expected because a nonhardened process was used for gate-oxide fabrication. Reducing the gate oxide thickness from 35 to 25 nm for SIMOX devices significantly improves the hardness. We previously have demonstrated a total-dose hardness up to $10^7\ \text{rad}$ for ZMR SOI/CMOS devices with a gate oxide about 10 nm thick.⁵

Table 3-3 summarizes the total-dose failure thresholds at which logic errors occur for gate arrays, divide-by-32 circuits and SRAMs. Circuit failure generally results from: (1) shift in n-channel V_T to a too small or negative value, (2) reduction in p-channel drive current because V_T becomes more negative, or (3) reduction in both n- and p-channel drive currents because mobility is degraded by interface-state generation. Consistent with the results shown in Figure 3-3, the 35-nm SIMOX circuits have the lowest failure thresholds, while the 25-nm SIMOX circuits generally have the highest. For divide-by-32 circuits, the failure thresholds depend upon whether tests are performed under static or dynamic conditions. In static tests, those devices that are biased under worst-case conditions (such as the 'ON' state for n-channel devices) can degrade rapidly (for example, by a large V_T shift as shown in Figure 3-5), leading to

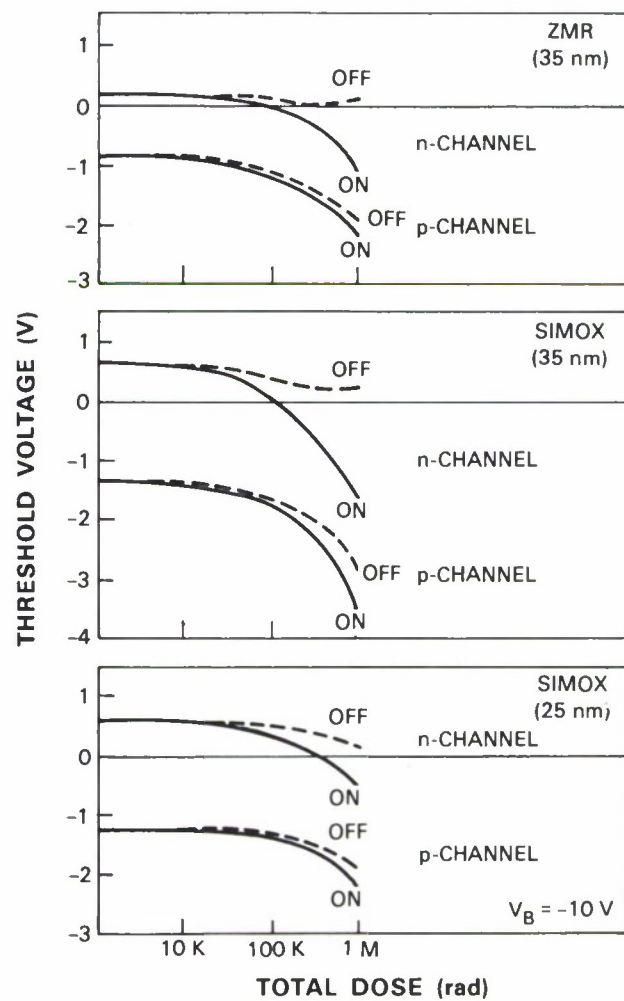


Figure 3-5. Threshold voltages of SOI/CMOS devices as a function of total dose.

TABLE 3-3 Total-Dose Failure Threshold for ZMR and SIMOX Circuits			
	ZMR (35 nm)	SIMOX (35 nm)	SIMOX (25 nm)
Gate Array	140 krad	80 krad	300 krad
1/32 Divider (Static)	130 krad	100 krad	400 krad
1/32 Divider (Dynamic)	> 1 Mrad	140 krad	700 krad
SRAM	60 krad	20 krad	70 krad

circuit failure. In dynamic tests, however, during which devices usually are switched between 'ON' and 'OFF' states, the rate of device degradation is reduced and the circuit failure threshold therefore is increased.

B-Y. Tsaur	C.K. Chen
V.J. Sferrino	R.W. Mountain
H.K. Choi	

REFERENCES

1. Solid State Research Report, Lincoln Laboratory, MIT (1986:2), p. 21.
2. Solid State Research Report, Lincoln Laboratory, MIT (1985:4), p. 28, DTIC AD-A172872
3. J.C.C. Fan, B-Y, Tsaur, and M.W. Geis, J. Cryst. Growth **63**, 453 (1983).
4. G.E. Davis, L.R. Hite, T.G.W. Blake, C-E, Chen, H.W. Lam, and R. DeMoyer, Jr., IEEE Trans. Nucl. Sci. **NS-32**, 4432 (1985).
5. B-Y, Tsaur, R.W. Mountain, C.K. Chen, G.W. Turner, and J.C.C. Fan, IEEE Electron Device Lett. **EDL-5**, 238 (1984).

4. MICROELECTRONICS

4.1 MBE-GROWN INSULATING GaAs USED AS MESFET BUFFERS

GaAs grown by molecular beam epitaxy (MBE) on GaAs substrates at low substrate temperatures (159°-300°C) is found to be electrically insulating and optically inactive. Yet, GaAs grown at normal growth temperatures (560°-620°C) on top of the low temperature GaAs (LT-GaAs) layer is crystalline and is of comparable quality with GaAs grown on semi-insulating GaAs (SI-GaAs) substrates. Research has begun on the growth, characterization, and device applications of LT-GaAs. MESFETs fabricated with LT-GaAs buffer layers have less leakage, resulting in approximately 20% higher breakdown voltages, and exhibit little or no light sensitivity. In addition, devices using LT-GaAs buffer layers have microwave gains (g_m) and high-frequency cutoffs (f_T) comparable with similar devices fabricated on SI-GaAs substrates. Current work is focusing on the characterization of the growth of LT-GaAs and measurements of backgating effects in MESFETs fabricated on LT-GaAs buffer layers.

F.W. Smith
C.L. Chen
A.R. Calawa

4.2 CHARGE-COUPLED DEVICE IMAGERS

We recently described¹ a charge-coupled device (CCD) imager that was designed and fabricated for the GEODSS (Ground-based Electro-optical Deep Space Surveillance) program. These devices consist of an array of 420×420 pixels and are front-illuminated through polysilicon gates. One requirement of these imagers is that they can be abutted to two other imagers on two adjacent sides to form a 2×2 focal plane array. We describe here a method of precisely aligning and assembling such focal plane arrays.

Figure 4-1 illustrates how the four 420×420 -pixel CCDs are arranged to form the focal plane array. There are three principal requirements placed on the assembly of this array. First, the pixel arrays of all four devices must be aligned mutually within the device plane to an accuracy of a small fraction of the pixel dimension, and, furthermore, the gap or 'seam loss' between imagers must be an integral number of two pixels. This requirement ensures that the focal plane pixels are all aligned to a common grid and obviates the need for expensive, off-focal plane processing to construct a geometrically corrected image from the four video signals. Since the pixel dimensions are $27 \times 27 \mu\text{m}$, alignment accuracies of a few micrometers are needed. The second requirement is that the planarity of the focal plane be better than $10 \mu\text{m}$. This need originates in the fact that the focal plane is to be attached by an optical cement to an optically flat fiber-optic bundle. The radiation emerging from the fibers has a low f-number (on the order of 2 to 3), and this requires the CCD surface to be within $10 \mu\text{m}$ of the bundle in order to minimize optical crosstalk between adjacent pixels. The final requirement is that the seam loss be as small as possible to minimize loss of targets that, for this application, can occupy a single pixel.

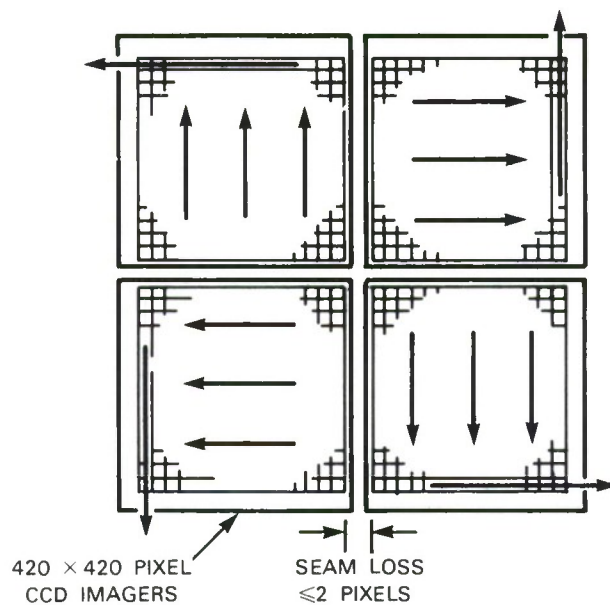


Figure 4.1. Abutted four-chip imager mosaic.

Minimizing the seam loss requires careful techniques for separating the individual wafer die without damaging the pixels in proximity to the edges. We use a Disco dicing saw with a diamond-impregnated blade to saw the wafer. This blade must undergo an extensive dressing procedure before use in order to minimize chipping damage to the devices. Our goal is to achieve a seam loss of two pixels, and this implies a strip of $27\text{-}\mu\text{m}$ maximum width from chip edge to pixel edge in which to place the saw cut. This width is reduced considerably by a number of factors, including allowances for errors in saw positioning, chipping, and the fact that there is an n^+/p junction between the chip edge and the outermost pixels to collect excessive generation current caused by saw damage.

The assembly of the four-chip array is illustrated in Figure 4-2. The CCD chips are held by a vacuum chuck, which in turn is mounted on a precision translation stage. A glass photomask is positioned just above the chuck and provides a flat mounting surface to which the dies are attached temporarily. The photomask has a series of lines defined in a thin film of chromium that serves as alignment marks. As the chuck is raised and the chip approaches the bottom of the photomask, the operator positions the n^+ collection diode under the alignment lines. When this alignment is satisfactory, the chuck is raised slightly, bringing the chip into physical contact with the photomask. To hold the chip in place, a few drops of a cyanoacrylate cement are placed in a series of small holes in the photomask (not shown in Figure 4-2) over the center of the chip. This cement spreads by a wicking action over the most of the die surface to form a thin bonding layer. After the four chips have been attached, a gold-plated Kovar plate (which will become the bottom of the final device package) is attached to the bottom (exposed) surface of the chips by

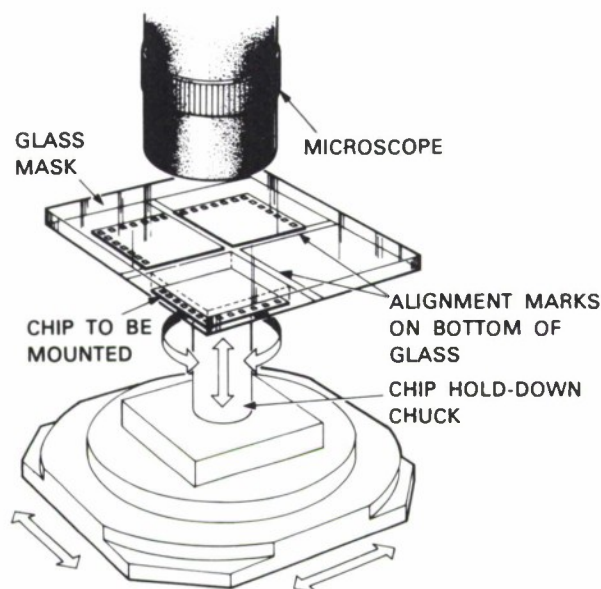


Figure 4.2. Assembly of four-chip array.

means of a layer of conductive epoxy. After the epoxy is cured, the cyanoacrylate is dissolved by a prolonged soaking in acetone, allowing the photomask to be separated from the CCDs. The package lead frame then is attached to the Kovar base, and the CCDs are wire-bonded to complete the assembly. A photograph of a completed four-chip focal plane is shown in Figure 4-3.

We have been able routinely to achieve alignment accuracies of less than $1\text{ }\mu\text{m}$ in the plane of the devices. This can be verified easily by examining the registration of the n^+ diode to the Cr alignment lines before the chips are demounted from the photomask. The planarity is measured by examining the four seams under a microscope having a shallow depth of focus and looking for height differences between the two-chip surfaces. In our case, this method has a resolution of about $3\text{ }\mu\text{m}$. We typically find no discernible variation in height across the seams, and this indicates that we are well within the planarity requirements imposed by the fiber-optic bundle. Although we have had some success in meeting the goal of a 2-pixel seam loss, this requirement has, to date, been the most difficult to achieve, mainly because of chipping problems and because the positioning accuracies required of the saw are close to the limits of that instrument. We have, however, fabricated a number of functioning focal planes with four-pixel gaps, and are continuing our efforts to achieve the two-pixel goal reproducibly.

P.J. Daniels
B.E. Burke

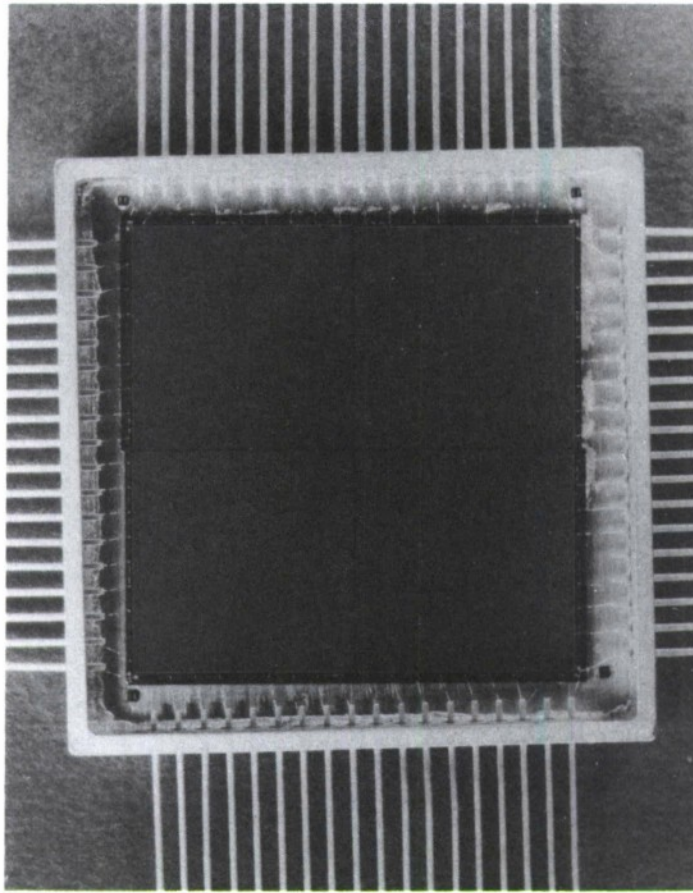


Figure 4.3. Completed four-chip array.

4.3 WAFER THINNING PROCESS

We have developed a thinning process that selectively etches the p^+ bulk and retains the active $10\text{-}\mu\text{m}$ -thick p^- epitaxial layer of the epitaxial wafers originally $500\text{ }\mu\text{m}$ thick. These layers will be used for back-illuminated CCD imaging devices.

Wafers to be thinned are mounted on substrates with the p^+ bulk on the back exposed. The back side is lapped and polished mechanically until the wafer is approximately $50\text{ }\mu\text{m}$ thick. Then a selective etch is used to remove the remaining p^+ bulk stopping at the p^- epitaxial layer.

The selective etch consists of eight parts of acetic acid, three parts of nitric acid and one part of hydrofluoric. When agitated in the ultrasonic solution, the etching ratio of the p^+ bulk (0.01 ohm-cm) to p^- epitaxial layer ($30\text{--}40\text{ ohm-cm}$) can be as high as 100 to 1. We now are optimizing the process variables (ultrasonic power, frequency, solution temperature, and mixture ratios) to maximize the selectivity and minimize the ultrasonic-induced defects.

The most important finding is that point defects in the bulk have resulted in shallow etch pits on the final epitaxial layer below the point defects. These point defects are caused by oxygen precipitating inside the p^+ bulk during the thermal cycles of the epitaxial growth. Figure 4-4 shows the point defects on the p^+ bulk manifested by the selective etch, and Figure 4-5 shows the

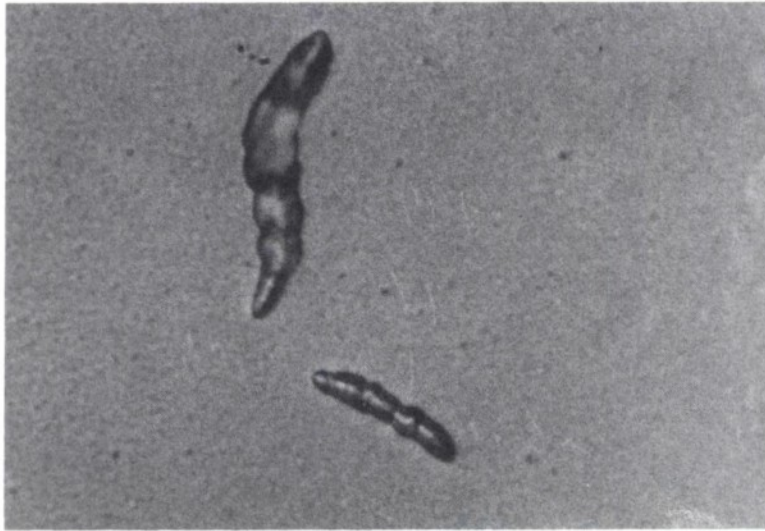


Figure 4.4. 140X photograph showing the point defects caused by oxygen precipitation in the bulk.

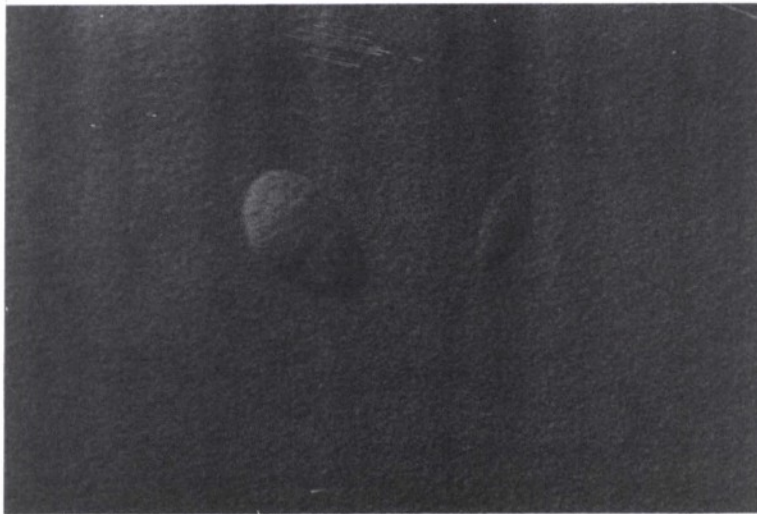


Figure 4.5. 780X photograph showing shallow etch pits on the epitaxial layer due to the point defects in the bulk.

shallow etch pits in the epitaxial layer that correspond to the point defects in the bulk. Thus, prior to epitaxial growth, it is necessary to preheat the substrate wafers to diffuse the oxygen from the surface, creating a denuded zone free of oxygen 60- μm deep below the surface. The oxygen in the bulk then must be precipitated so it will not diffuse to the denuded zone in later processes.

J.C.M. Huang

4.4 ATTAINMENT OF 0.13- μm LINES AND SPACES BY EXCIMER-LASER PROJECTION LITHOGRAPHY

In the context of evolving submicrometer lithographies, including X-ray and ion-beam techniques, it is of interest to determine the practical limits of deep-UV projection lithography. It now is widely believed that the next UV optical lithography will make use of an excimer laser source.^{2,3} However, important questions remain about how these sources can be incorporated into projection (optical stepper) lithography, and therefore, about the ultimate resolution of these optical techniques.

In the present experiments, we have explored high-resolution projection printing using reflective 0.5 numerical aperture (NA), 36:1 reduction optics in the geometry described in Reference 2. For a study of the resolution capabilities of our system, we have chosen hard 'diamond-like' carbon resists that are exposed by single 2-ns ArF laser pulses in a self-developing response as previously described.⁴ Thin resist films of 100- to 200-nm thickness were applied by RF plasma deposition from butane onto Si and GaAs substrates and exposed with excimer pulses attenuated to fluences of 0.1 to 1 J/cm².

Figure 4-6 shows SEMs of 0.13- μm lines and spaces patterned in projection onto hard carbon resist on GaAs. The fluence, ≈ 0.2 J/cm², was near threshold for ablation, and its effect was 'blistering' of the carbon, which was nevertheless sufficient for further preferential dry etching of the GaAs substrate. The projected 0.13- μm -wide lines are significantly smaller than the wavelength of the laser, $\lambda = 0.193$ μm , and, in fact, approach the absolute diffraction-limited cutoff width $\lambda/4\text{NA} = 0.097$ μm . In separate studies, we determined the order of nonlinearity ψ^* , which characterizes the response of the hard carbon film to excimer irradiation. High contrast, $\psi^* = 22$, was obtained for 100-nm-thick films under self-development conditions. Our results show that, even with limited control of the aberrations in the projection optics, 0.13- μm lines and spaces can be generated in projection with the appropriate choice of system parameters. Keys to optimal performance are: single-pulse exposure, a high contrast response, and built-in 'bleaching' via saturation of the resist response at high exposure.

M. Rothschild

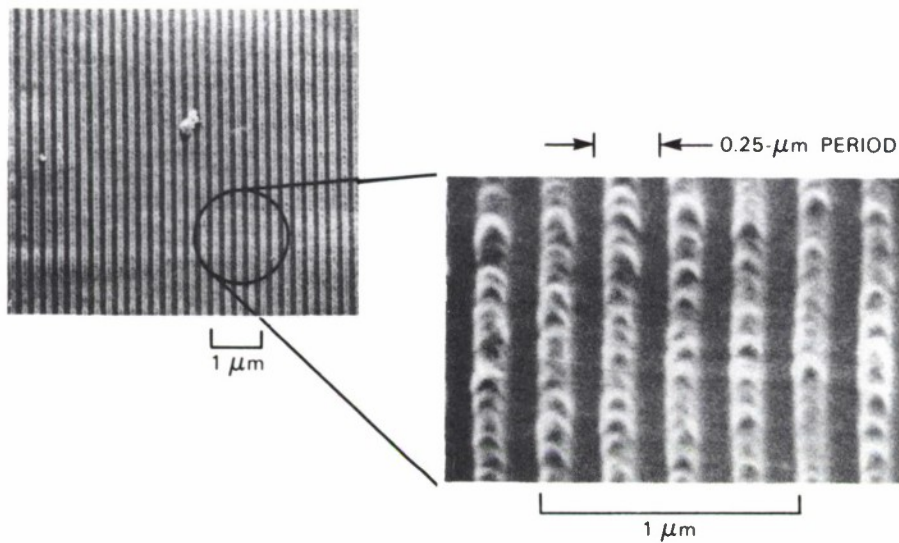


Figure 4.6. SEMs taken at two different magnifications of 0.13- μm lines and spaces on carbon resist on GaAs (one 193-nm pulse, $\sim 0.2 \text{ J/cm}^2$ fluence).

4.5 OBSERVATION OF MILLIMETER-WAVE OSCILLATIONS FROM RESONANT-TUNNELING DIODES AND SOME THEORETICAL CONSIDERATIONS OF OSCILLATION-FREQUENCY LIMITS

The resonant-tunneling diode (RTD) has attracted attention since the first observations of negative differential conductance (NDC). As shown in Figure 4-7, this NDC is a consequence of the spatial quantization that occurs in a thin quantum well surrounded by thin potential barriers. Interest in the RTD increased greatly with the first measurement of the response time of the NDC, $\tau \leq 100 \text{ fs}$.⁴ Most of the present interest stems from a desire to construct very high speed two-terminal oscillators for millimeter- and, it is to be hoped, submillimeter-wave applications. We recently have made significant progress toward this end by achieving the first millimeter-band oscillations with resonant-tunneling diodes at room temperature. Fundamental frequencies up to 56 GHz have been observed, while relatively powerful second harmonic frequencies have been seen up to 87 GHz. In a parallel effort, several theoretical calculations have been performed to predict the maximum oscillation frequency, f_{max} , obtainable with the resonant-tunneling diode. Several of these calculations actually predict maximum frequencies far lower than we already have observed. This section analyzes the various calculations in light of our most recent experimental results.

Table 4-1 summarizes the oscillation results achieved to date with three different RTD devices along with the important material and electrical parameters for each device. The observed oscillation frequency, f_{osc} , is determined largely by the waveguide resonator structure and is discussed at length elsewhere.⁵ The electrical parameters are used to calculate the maximum

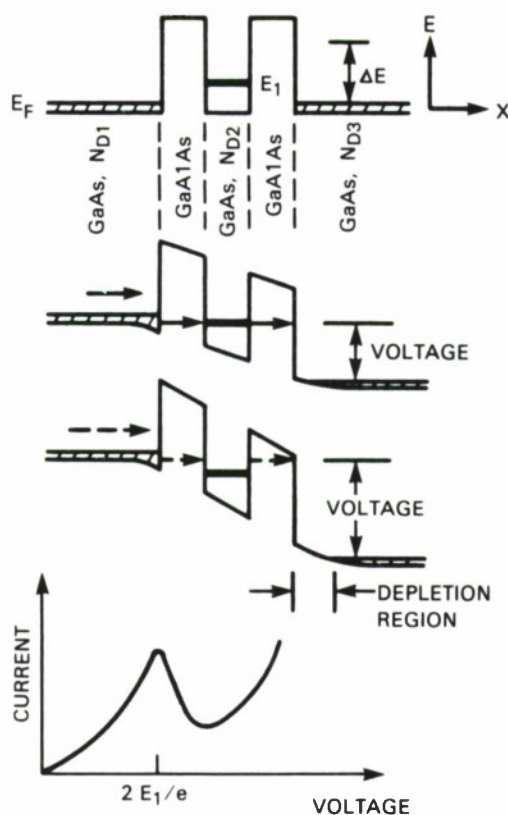


Figure 4.7. Current-voltage curve of double-barrier diode.

oscillation frequency allowed by parasitics,⁶ f_p . This calculation assumes that the RTD can be modeled as the parallel combination of a capacitance, C , and a negative conductance, G , in series with a resistance, R_S . The capacitance of each device was obtained from a separate band-diagram calculation, and negative conductance was obtained experimentally. The series resistance also was calculated, but was measured in one sample and found to agree with the calculation. Notice that the values of f_p are all greater than f_{osc} . For sample 1, this frequency limit explains our inability to make the device oscillate near 40 GHz.⁵

Closely associated with the parasitics is the transit time across the depletion region. Longer depletion regions reduce the capacitance of the device, but also introduce a phase shift in the current relative to the applied voltage, just as would charge storage in the well. While this phase shift could be used as the basis for a transit-time oscillator similar to a BARITT diode, we will assume here that the phase shift must be kept small to utilize the negative conductance. This time delay, τ_D , yields a maximum frequency which we define as $f_D = (2\pi\tau_D)^{-1}$. Assuming a carrier saturation velocity of 1×10^7 cm/s, we calculate the limits that appear in Table 4-1. Note that it is significantly higher than the observed oscillation frequencies.

TABLE 4-1
Resonant Tunneling Diode Parameters

	Sample		
	1	2	3
MATERIAL PARAMETERS			
Barrier Metal	AlAs	Ga _{0.7} Al _{0.3} As	AlAs
Barrier Thickness (nm)	2.5	3.0	1.5
Well Thickness (nm)	4.5	4.5	4.5
Doping Outside Barriers (cm ⁻³)	1×10^{18}	2×10^{17}	1×10^{17}
ELECTRICAL PARAMETERS			
Peak-to-Valley Ratio	1.7/1	1.3/1	3.5/1
Peak Current Density ($\times 10^4$ A cm ⁻²)	0.8	1.2	4.0
Depletion Length at Bias for NCD (nm)	15	30	90
Capacitance (fF) [1]	100	50	16
Maximum Negative Conductance (mS) [1]	5.0	8.0	13.0
Series Resistance (Ω) [1]	10	15	15
OSCILLATION CHARACTERISTICS			
dc Bias I_B , V_B (mA,V)	0.7, 0.40	2.7, 0.32	3.0, 0.95
f_{osc} (GHz) [2]	20.7	43.7	56.4
P_{osc} (μ W) [3]	0.1	1.0	60.0
CALCULATED MAXIMUM OSCILLATION FREQUENCIES			
f_p (GHz) [4]	34	69	263
f_D (GHz) [5]	1000	500	180
f_{WKB} (GHz) [6]	0.01	220	6.0
f_L (GHz) [7]	0.01	60	6.0
f_{KD} (GHz) [8]	140	300	130

- [1] Typical values for a circular mesa of 4- μ m diameter.
[2] Maximum observed fundamental oscillation frequency.
[3] Output power at f_{osc} .
[4] $f_p = (2\pi C)^{-1} (G_{max}/R_S - G_{max}^2)^{0.5}$.
[5] WKB estimate of charge storage time in quantum well.
[6] From Reference 7.
[7] From Reference 8.
[8] From Reference 9 for electron lifetime in well with infinitely thick barriers.

One way to perform a completely theoretical calculation of f_{\max} is to assume that this frequency is determined only by the amount of time required for an electron to escape from the quantum well. Bohm⁷ has solved this problem in the WKB approximation and found the escape time to be given approximately by the classical period in the well divided by the transmission probability of a barrier, i.e., $\Delta t = [\theta^2 + (16\theta^2)^{-1}]\tau \approx \theta^2\tau$, where τ is the classical period and θ^{-2} is the transmission coefficient, both calculated using the WKB method. In Table 4-1, the frequencies associated with Δt , $f_{\text{WKB}} = (2\pi\Delta t)^{-1}$, are all well below the observed frequencies, indicating something wrong with the theory. The problem is that the WKB method is inaccurate because the DeBroglie wavelength of the electrons in the well is longer than the spatial extent (i.e., barrier width) over which the potential varies.

Another way to estimate f_{\max} is to assume that it is determined entirely by the tunneling resistance and capacitance associated with the leading barrier of the RTD. Luryi⁸ adopted this approach, calculating the dynamic tunneling resistance using the WKB method and the capacitance from the parallel plate model. As seen in Table 4-1, the resulting frequency, $f_L = (2\pi RC)^{-1}$, is far less than the observed oscillation frequency for two diodes. This discrepancy is at least in part because of the WKB approximation, which almost certainly overestimates the tunneling dynamic resistance.

Perhaps a more realistic estimate of f_{\max} can be derived from an exact (numerical) solution to the time-dependent Schrodinger equation for a thin quantum well performed by Kundrotas and Dargys.⁹ These authors solved for the time of escape from a delta-function quantum well after the application of an electric field. They found this time to be significantly shorter than that obtained by all standard approximation methods. It is interesting to note that their results yield a cutoff frequency, labeled f_{KD} in Table 4-1, that is much higher than the f_{WKB} even though the barriers in their model are infinitely thick. For our thin barriers, one would expect the escape time to be considerably shorter, with an accompanying increase in f_{\max} .

In conclusion, our experimental results on double-barrier diode oscillations provide strong evidence that the intrinsic limit on oscillation frequency is much higher than predicted by approximations using the WKB method. The frequency limit, f_{KD} , is probably closer to reality than all the WKB estimates yet is still very conservative. At this point in the development of RTD oscillators, we believe that the parasitics present the first hurdle to higher frequencies, and that these must be optimized with the depletion layer drift time in mind. There appear to be no fundamental or practical impediments to obtaining RTD oscillations up to several hundred gigahertz.

T.C.L.G. Sollner	W.D. Goodhue
E.R. Brown	H.Q. Le

REFERENCES

1. Solid State Research Report, Lincoln Laboratory, MIT (1985:1), p. 31, DTIC AD-A160922.
2. D.J. Ehrlich, J.Y. Tsao, and C.O. Bozler, J. Vac. Sci Technol. **B3**, 1 (1985).
3. M. Rothschild, C. Arnone, and D.J. Ehrlich, J. Vac. Sci. Technol. **B4**, 310 (1986).
4. T.C.L.G. Sollner, W.D. Goodhue, P.E. Tannenwald, C.D. Parker, and D.D. Peck, Appl. Phys. Lett. **43**, 588 (1983).
5. E.R. Brown, T.C.L.G. Sollner, W.D. Goodhue, and C.D. Parker (to be published).
6. M.E. Hines, Bell Syst. Tech. J. **39**, 477 (1960).
7. D. Bohm, *Quantum Theory* (Prentice-Hall, Englewood Cliffs, 1951).
8. S. Luryi, Appl. Phys. Lett. **47**, 490 (1985).
9. J. Kundrotas and A. Dargys, Phys. Status Solidi B **134**, 267 (1986).

5. ANALOG DEVICE TECHNOLOGY

5.1 HIGH-PERFORMANCE SUPERCONDUCTIVE CHIRP FILTERS

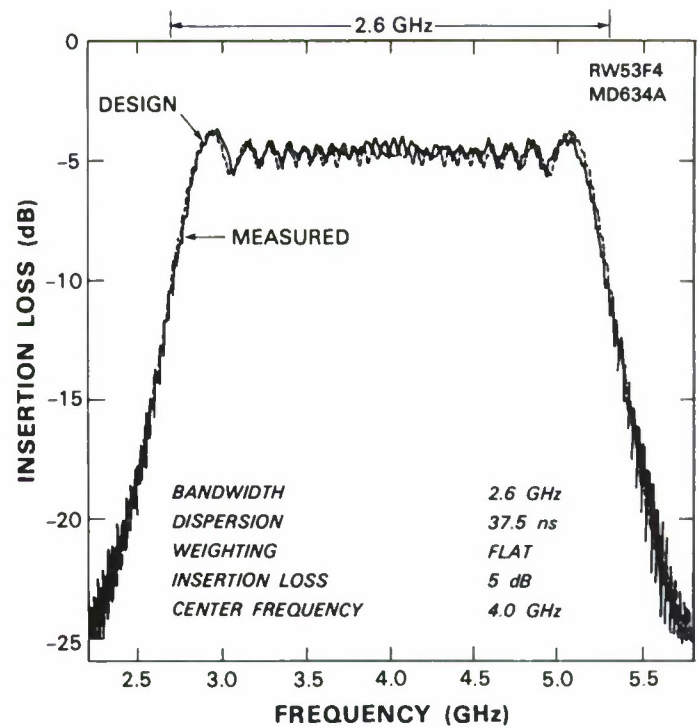
Superconductive chirp filters show substantial promise for wideband analog signal processing. Previously, pulse compression over a 2.3-GHz bandwidth was reported for a matched pair of devices, although nonidealities limited side-lobe performance.^{1,2} Recently, improvements to the fabrication and packaging processes have led to high-performance chirp filters that exhibit excellent compressed pulse responses.

The superconductive chirp filters consist of tapped electromagnetic delay lines that employ a cascade of backward-wave couplers.³ The wide bandwidth, along with low-loss delay and accurate tapping functions, is provided by thin-film superconducting niobium striplines patterned on thin silicon substrates.⁴ The chirp filters are designed to have 37.5 ns of dispersion and a 2.6-GHz bandwidth (centered at 4 GHz), for a time-bandwidth product of 98. The filter response can be amplitude-weighted by varying the strength of the backward-wave couplers along the length of the device. For pulse compression, two types of chirp filters were designed. One filter has a flat, 5-dB insertion loss across the design bandwidth, while the other filter is weighted for a Hamming response with a 5-dB insertion loss at the center frequency.

In the past, the chirp filters had been designed to have a 10-dB insertion loss. The stronger coupling in the present design is expected to improve the ratio of desired to spurious signals of the compressed-pulse response, although at the expense of limiting the theoretical side-lobe performance. The higher-insertion-loss designs were unable to reach their potentially superior side-lobe performance because of spurious signal reflections stemming from particle contamination within the device. An important factor in improving the present device lies in refining the fabrication process to reduce the presence of dirt, which can alter the stripline impedance sharply and seriously degrade device performance. The RF packages that contain the chirp filters also have been modified to prevent particulates from entering subsequent to the packaging process.

The CW phase and amplitude responses of the chirp filters were measured from 2 to 6 GHz using an automatic network analyzer. Both the measured and simulated amplitude responses of a flat-weighted device are shown together in Figure 5-1. The simulations were made with the first-principles theory used to design the filter and were based on the physical design parameters of the device. The agreement between theory and experiment is excellent, even to the Fresnel ripple, which is strongest at the frequency-band edges. Figure 5-2 shows the measured and simulated phase deviation from the best-fit quadratic. The measured best-fit quadratic yields a chirp slope that is within 1.3 percent of the designed chirp slope. The remaining phase error (deviation from quadratic) has an rms value of 6.0° , which is very close to the predicted rms phase error of 5.9° . Note that the measured phase-deviation data closely tracks the simulated phase deviation, especially along the large amplitude swings near the band edges that are a consequence of the Fresnel ripple.

Figure 5-1. Insertion loss vs frequency of a flat-weighted superconductive chirp filter.



76401-41

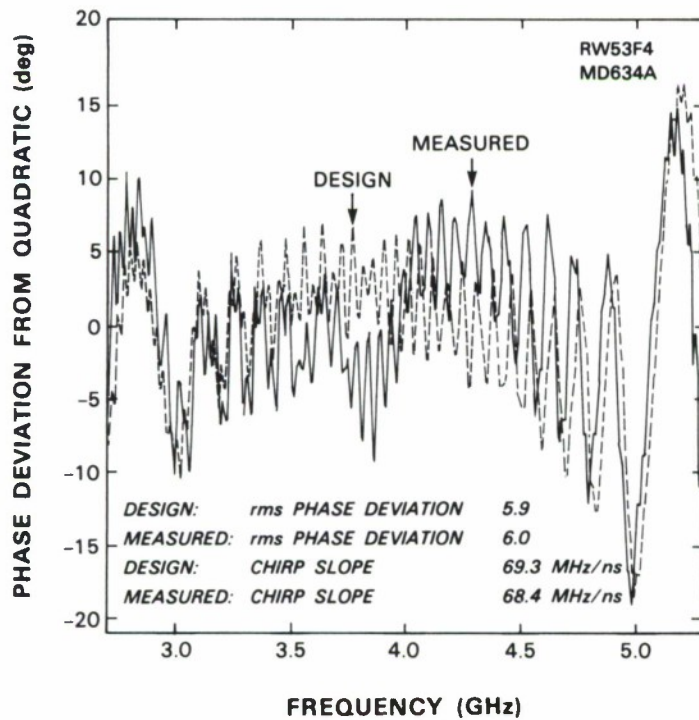


Figure 5-2. Phase error (deviation from best-fit quadratic) of a flat-weighted superconductive chirp filter.

76401-42

The measured and simulated amplitude responses of a Hamming-weighted filter are shown in Figure 5-3. Again, the agreement is excellent. The phase deviation from quadratic is shown in

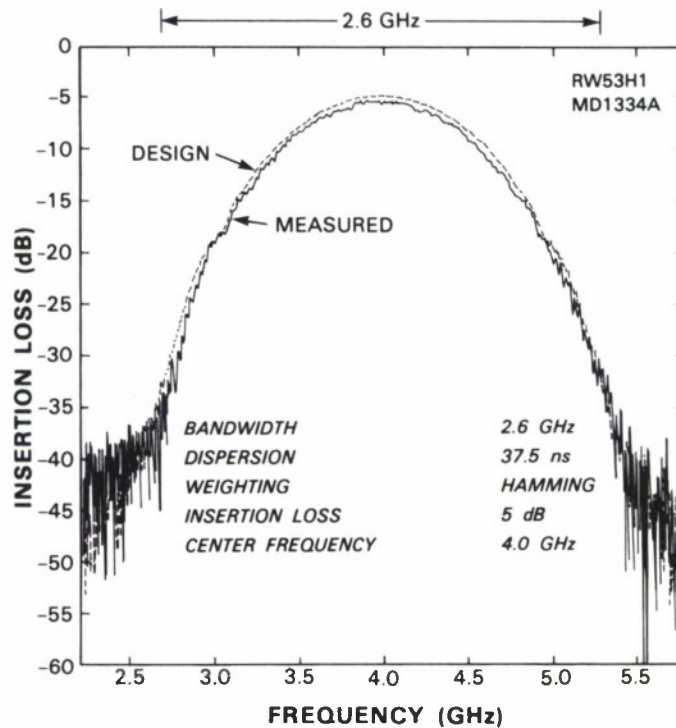


Figure 5-3. Insertion loss vs frequency of a Hamming-weighted superconductive chirp filter.

Figure 5-4. The measured chirp slope differs from the design value by 0.8 percent. The measured rms phase error has been weighted by the Hamming function to yield a weighted rms phase error of 3.3° , which compares favorably with the predicted weighted rms phase error of 3.5° . For comparison, the measured unweighted rms phase error is 5.0° while the predicted unweighted rms error is 3.9° . The slowly varying sinusoidal shape of the phase deviation data stems from the strong coupling of the taps. The higher frequency swings at the edges of the band result from the Fresnel ripple, which is reduced in impact because of the Hamming weighting.

The compressed-pulse response of a matched pair of chirp filters was obtained by applying an 8-V video impulse of 90-ps width to the input of the flat-weighted filter. The expanded up-chirp response then was directly applied to the down-chirp input port of the Hamming weighted filter. Figure 5-5 shows the resulting compressed pulse, which has a 4-dB full width of 0.6 ns, consistent with the 2.6-GHz bandwidth and Hamming weighting. The largest side lobe lies at -29 dB relative to the central peak.

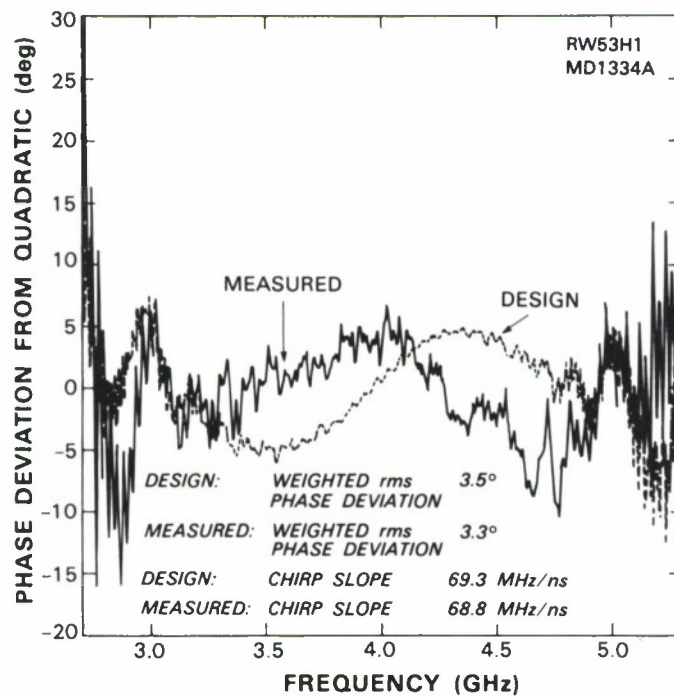


Figure 5-4. Phase error (deviation from best-fit quadratic) of a Hamming-weighted superconductive chirp filter.

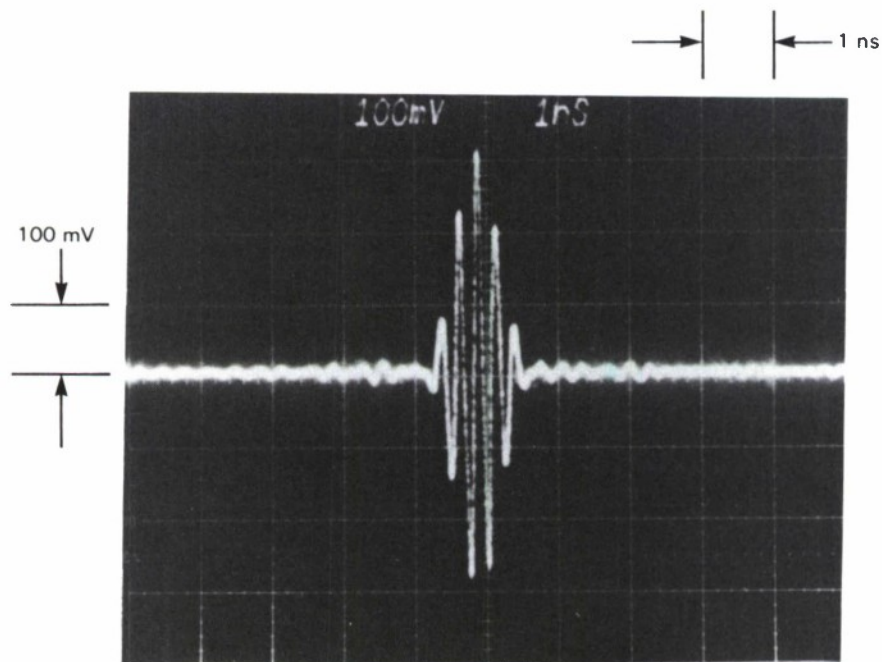


Figure 5-5. Compressed-pulse response of matched flat- and Hamming-weighted superconductive chirp filters.

The envelope of the compressed-pulse response expected from the data is shown in Figure 5-6. The transfer functions of the two filters (obtained from measured data such as shown in Figures 5-1 through 5-4) are multiplied and then Fourier transformed to generate the compressed-pulse response. Note that the 4-dB full width is 0.6 ns and the largest side-lobe level

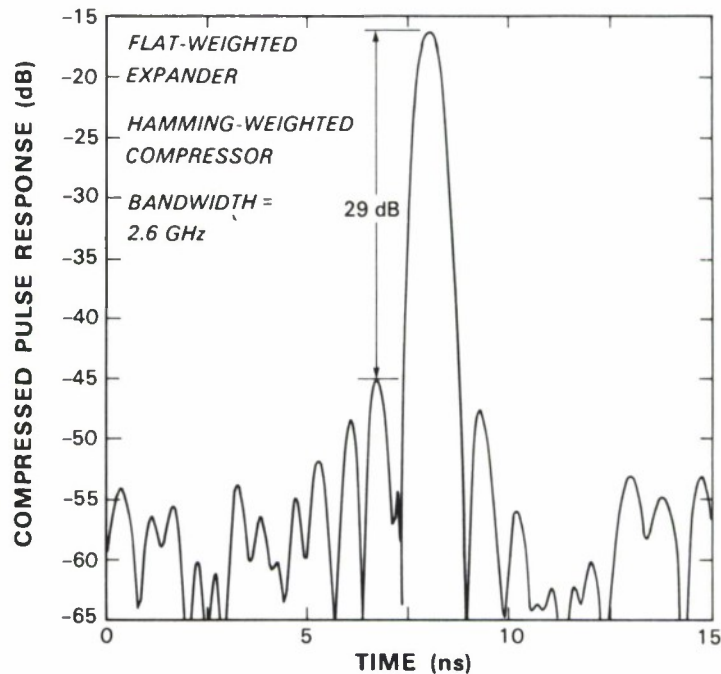


Figure 5-6. Compressed pulse response envelope generated from amplitude and phase data of same devices as in Figure 5-5.

is -29 dB, both in accordance with the time-domain measurement. The relative side-lobe level expected from the design is -30 dB. Note that to obtain the ideal -42-dB Hamming side lobes would require a design with higher insertion loss or with phase predistortion⁵ to compensate for the effects of strong tapping and the consequent input wave depletion.

In summary, pulse compression over a 2.6-GHz bandwidth has been demonstrated with a matched pair of superconductive chirp filters. Improvements to fabrication and packaging processes have yielded excellent devices that closely match the design. Preliminary measurements also have shown the packaging improvements to lend good thermal cyclability (room temperature to 4.2 K and back) to these devices.

M.S. DiIorio
R.S. Withers

5.2 SUPERCONDUCTIVE DELAY LINE WITH INTEGRAL MOSFET TAPS

Superconducting tapped delay lines have been fabricated previously with mask-programmable tap weights.¹⁻⁵ MOS transistors, however, can provide the variable conductance needed to programmably weight the tapped outputs. On this basis, we have built a prototype circuit (Figure 5-7) to demonstrate the feasibility of processing and operating transistors (MOSFETs) with a superconducting microstrip tapped delay line on the same silicon wafer.⁶

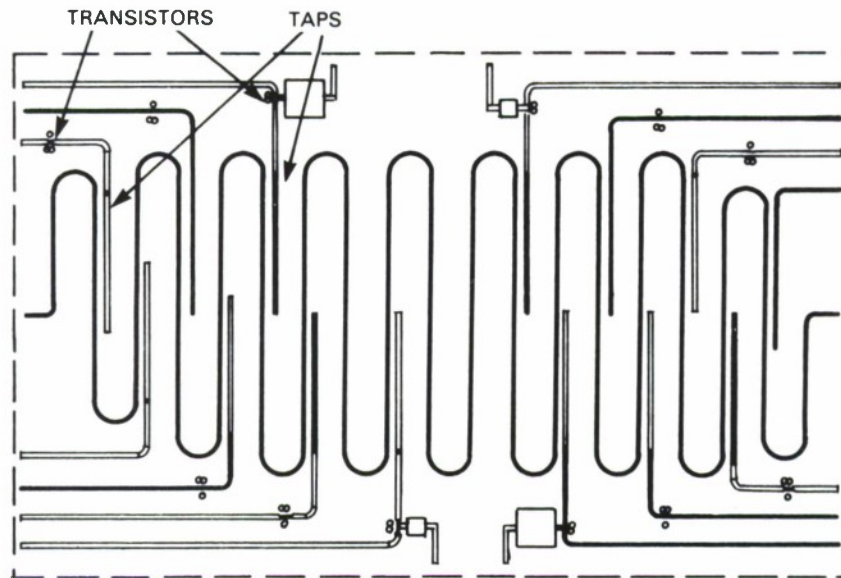


Figure 5-7. Mask layout of the programmable tapped delay line showing transmission line, taps, and transistors. The niobium areas are filled and the aluminum areas are open. The large aluminum capacitors attached to four of the transistors are bypass capacitors to ground to reduce feedthrough.

The high-temperature MOS processing preceded the temperature-sensitive superconducting niobium processing. A dual-dielectric gate of SiO_2 and Si_3N_4 for self-alignment of the source and drain with respect to the gate dielectric was used for the n-channel MOSFETs. The bird's-beak encroachment of the oxide over the source and drain under the gate dielectric reduces the parasitic gate-source and gate-drain capacitances. To ensure that the p^+ areas remained degenerate (which is necessary for conduction at 4.2 K), the n^+ source/drain diffusion was done before the p^+ isolation diffusion. Boron is very soluble in SiO_2 , so the silicon surface becomes depleted of boron during any high-temperature steps following this diffusion. Aluminum and niobium were used alternately for both gates and source/drain contacts. The superconducting niobium was sputter deposited and reactive-ion etched to form the microstrip delay line and taps as well as some of the gates and contacts. CF_4 was chosen to etch niobium over aluminum selectively.

Both the aluminum-gate and novel niobium-gate transistors worked well at 4.2 K. Threshold voltages were approximately 0 V for aluminum-gate devices and -5 V for niobium-gate devices. The negative threshold shift for the niobium-gate devices is due to positive charge in the gate dielectrics caused by the high-energy niobium sputter deposition. (The aluminum-gate devices were protected at this point by aluminum.) Note that this threshold shift does not hinder the analog operation of these MOSFETs. At 4.2 K, channel mobility for all devices increased 3 to 5 times over expected room-temperature values to 2000-3500 cm²/V-s. No differences in contact resistance between niobium and aluminum source/drain contacts were discerned, indicating that niobium makes a low-resistance ohmic contact to phosphorus-doped silicon.

The high-frequency superconducting operation was evaluated using a stripline resonator and by measuring the tapped-delay-line/MOSFET circuit between 2 and 5 GHz. The best quality factors (Qs) of the resonator were just above 10,000, which are an order of magnitude lower than the Qs measured on resonators placed on unprocessed silicon, but are adequate for good device operation.

MOSFET performance as tap-weighting elements for high-frequency signals is illustrated in Figure 5-8. This frequency-domain measurement shows, with gate voltage as a parameter, the output at the drain of the MOSFET when a high-frequency signal is applied to the source of the device. The measurement demonstrates that the output signal is a function of the MOSFET channel conductance; when data is collected for measurements at 1-V increments in gate voltage over an 18-V range, a linear relation between gate voltage and tapped output is seen with an

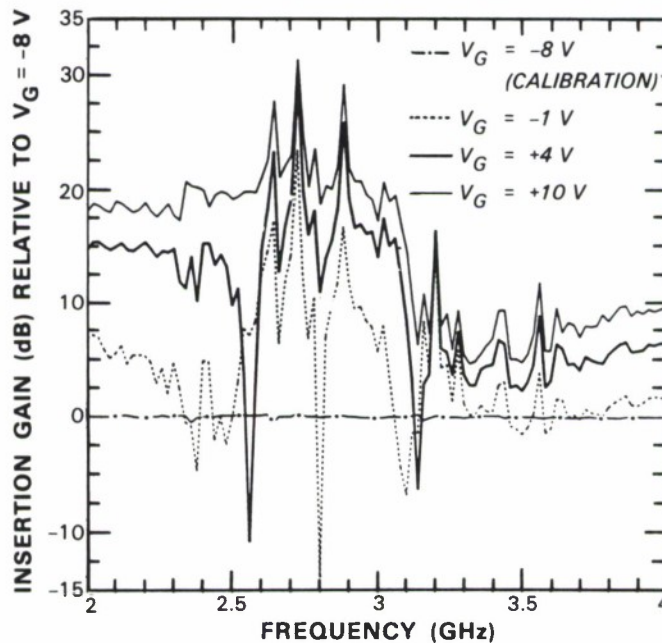


Figure 5-8. Normalized insertion gain measurements vs frequency, plotted for three different gate voltages. The curves plotted are normalized to the measurement at -8 V. The MOSFET controlling this tap does not have gate bypassing.

on/off ratio of 18 dB demonstrated between 2 and 2.4 GHz. In Figure 5-9, this data has been plotted at 2.2 GHz for a niobium-gate device. Similar results were obtained from time-domain-reflectometer (TDR) measurements where an impulse was sent into the source of the MOSFET

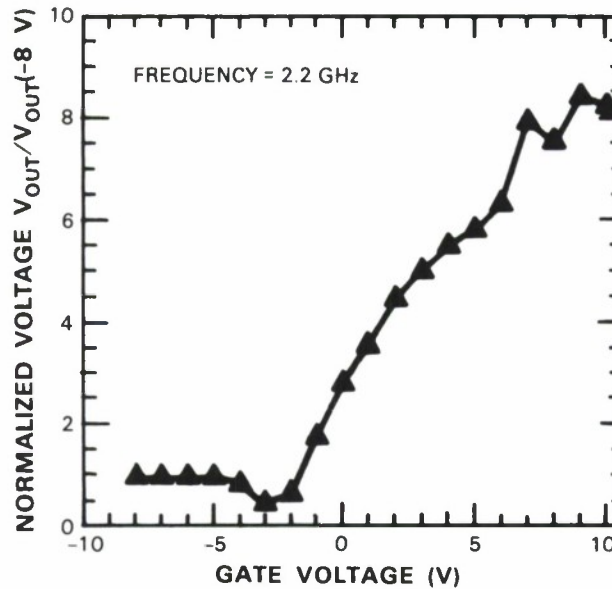


Figure 5-9. Measurement of the modulated channel conductance as a function of gate voltage for a tap controlled by a non-gate-bypassed Nb-gate transistor.

76401-34

and the resulting attenuation at the drain was measured as a function of gate voltage. Higher on/off ratio is expected from tapping MOSFETs with gates that are capacitively bypassed to ground, thereby reducing capacitive feedthrough, and wider-bandwidth operation is anticipated in a stripline version of the circuit, which will have less spurious reflection.

M.A. Delaney	J.B. Green
R.S. Withers	R.W. Mountain
A.C. Anderson	

5.3 FURTHER ASSESSMENT OF NONLINEAR ASSOCIATIVE MEMORY FOR DETECTING LINES IN IMAGES

We have studied a restricted pattern-recognition problem in which we attempt to detect the presence or absence of line patterns in an optical image that is corrupted by Gaussian additive noise. The detection probabilities for conventional two-dimensional matched filtering or template matching techniques are compared with those of several versions of nonlinear associative memory, which are one form of artificial neural-network techniques.

For N-pixel data fields, Hopfield's nonlinear associative memory processor⁷ forms an N-by-N association matrix directly from the outer products of the M individual binary-quantized line

pattern data vectors, $F^1 \dots F^M$. We have shown⁸ that this processor is equivalent to the schematic of Figure 5-10 in which the noise-corrupted input data field is convolved with the M ($= 3$ in this case) individual matched-filter masks for the noise-free input patterns. The

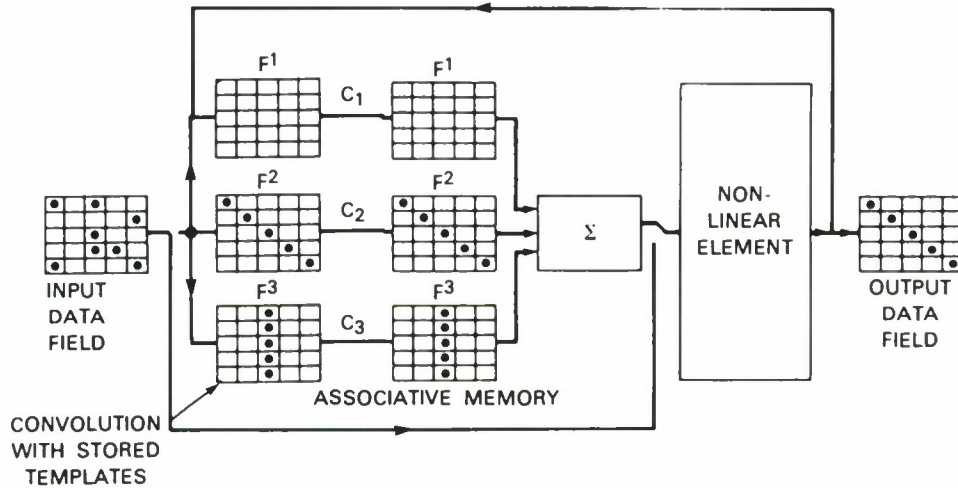


Figure 5-10. Hopfield memory.

resulting scalar outputs $C_1 \dots C_M$ then are multiplied by the same pattern data before pixel-by-pixel summation and application of the nonlinear operator. Matched filtering employs only the lefthand part of Figure 5-10, simply selecting the largest C_k value and identifying k as the input pattern.

We reported that superior associative memory performance could be achieved by replacing the lefthand set of F vectors in Figure 5-10 by B vectors⁸⁻⁹ that obey a mutual orthonormality relationship with the F vectors in order to minimize the cross-correlation terms. Although such B vectors previously were obtained by symmetry considerations, we subsequently have derived the following general expression

$$B = F \cdot D^{-1}.$$

In this expression, $D = F^T \cdot F$ is the M -by- M correlation matrix for the F vectors, where the M individual patterns are represented as a single two-dimensional matrix F comprising M columns and N rows. The inverse of the D matrix will exist provided the F vectors are linearly independent. This solution turns out to be the optimal linear association matrix. A more general solution using Moore-Penrose matrix inversion treats the case where the F vectors are linearly dependent.¹⁰

Simulations were run on 9-by-9-pixel data fields.⁸ The initial input states for the simulations were generated by taking an ideal input pattern and adding analog, Gaussian-distributed noise to each binary pixel value for an SNR of 3.5 dB. Simulations were performed with up to eight

different line orientations in addition to the no-line state. Figure 5-11 summarizes the results by plotting the probability of detection against the number of ideal patterns for several types of processors. This shows separately the results for a noisy no-line input pattern and the noisy line

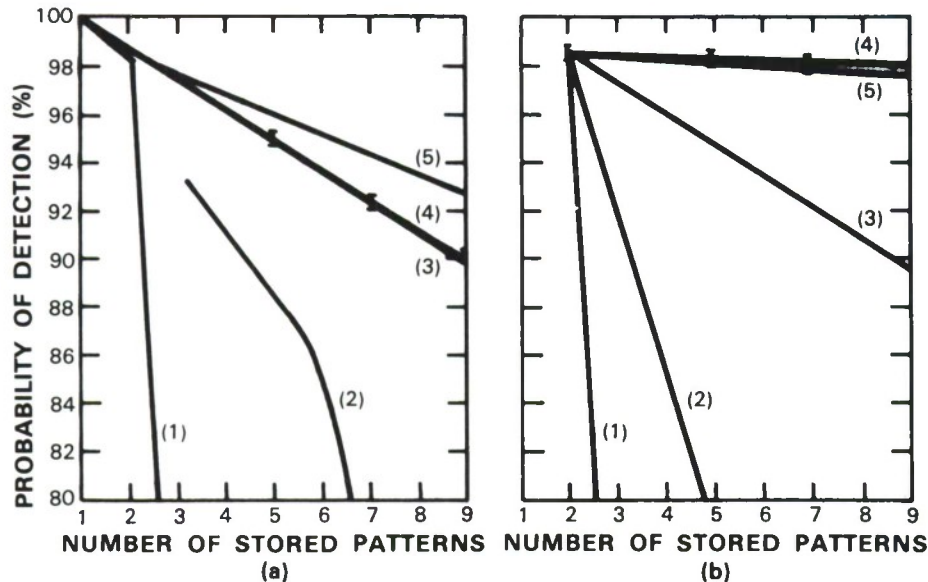


Figure 5-11. Recognition of (a) no-line and (b) line patterns in 9-by-9 images using various processors: (1) unmodified Hopfield, (2) Hopfield with orthonormal basis vectors, (3) orthonormal basis vectors and analog processing on first pass, (4) matched filter, and (5) Hopfield with orthonormal basis vectors and analog processing using an offset sigmoid nonlinear operator.

patterns. The types of processors are: (1) the Hopfield processor, which uses binary input data in which the noisy analog data were quantized to values of -1 or $+1$ before submitting them to the processor (Figure 5-10), (2) the Hopfield processor, with the association matrix formed from the orthonormal B vectors, and using binary-quantized data throughout, (3) the processor of (2) but with the original analog input data supplied for the first pass through the associative memory, and (4) the matched-filter processor. These simulations clearly show that the Hopfield associative memory is inadequate for our problem. The performance with orthonormal basis vectors [curve (2)] is better but only becomes acceptable when the analog data is preserved for the first pass through the processor [curve (3)].

The performance in Figure 5-11 was considered to be acceptable only for the no-line case. When detecting noise-corrupted line patterns, the simulations still exhibited occasional errors in which they settled into a state that is a superposition of two line patterns. There was a progressive increase in the number of such errors when a larger number of line patterns was stored (Figure 5-11). We therefore examined a more elaborate processor design in an attempt to improve the associative-memory performance level. We ultimately selected a continuous sigmoid-type nonlinear operator, comprising an inverse tangent function, scaled by $2/\pi$ to provide the

required output range from -1 to $+1$, whose steepness was increased with successive iteration. The best operator we examined, with sigmoids crossing the abscissa at an offset of $+0.05$, achieved the performance of curve (5) in Figure 5-11 that came closest to the matched-filter results. The effective improvement in no-line detection is a consequence of employing the offset operator that biases the output in favor of the no-line state, with a reduced detection performance for each of the M line patterns compared to the matched filter.

We also have assessed the relative fault tolerance of the associative memory in comparison with the matched filter. This was performed on the 5-by-5-pixel data fields with two distinct types of errors. Initially, we introduced Gaussian random noise into the stored matrix and matched-filter coefficients. Although the matched-filter template masks comprise only $+1/-1$ binary-quantized values, an investigation of the associative-memory matrix weight values showed them to vary in the range $+14.4/-1.6$, which required much higher dynamic range. This was compensated for in our simulations by introducing proportionately larger noise into the associative memory compared to the matched-filter processor. Figure 5-12(a) shows the probability of detection for a line pattern with various magnitudes of error with respect to the stored weight values. Figure 5-12(a) clearly shows the associative memory to be less fault tolerant. Figure 5-12(b) shows results when the errors are dropouts or faults where a weight position is totally inoperative. This simulation was found to be particularly sensitive to the positions of the dropouts, with a large spread in the plotted points even after measurements with several thousand random dropout patterns at a particular dropout percentage. It was concluded that there was little difference in the fault tolerance of the two approaches.

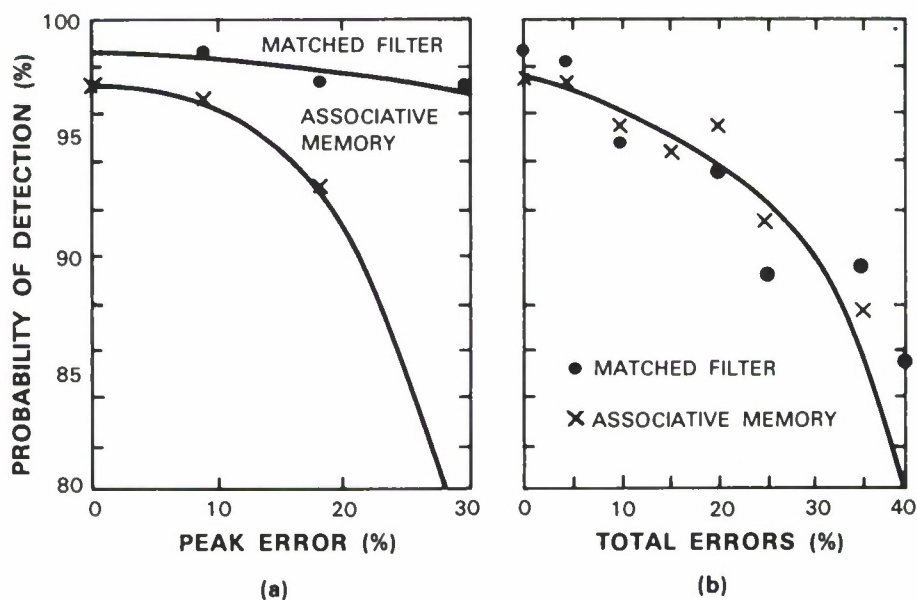


Figure 5-12. Line-detector performance for 5-by-5 images at +6-dB input SNR with (a) random additive errors in the processor coefficients, and (b) random dropouts of processor elements. The curves show averages over many processor error patterns.

We have concluded that, in our application, the associative memory is very sensitive to the choice of pattern data stored in the association matrix. The storage of orthonormal basis vectors was essential, but, even with these, the associative memory still possesses a considerable performance degradation compared to the matched-filter approach, unless a sophisticated nonlinear operator is used. However, the matched-filter techniques, besides offering greater computational efficiency and superior fault tolerance, can handle directly the analog pattern data and filter coefficient values that are required to process the output from practical optical imagers. Artificial neural-network-based processing appears to be better suited to the recognition of unknown patterns, where the processor has to learn the stored template data directly from the input data samples.

P.M. Grant
J.P. Sage

REFERENCES

1. J.T. Lynch, R.S. Withers, A.C. Anderson, P.V. Wright, and S.A. Reible, *Appl. Phys. Lett.* **43**, 319 (1983).
2. Solid State Research Report, Lincoln Laboratory, MIT (1983:4), p. 59, DTIC AD-A142991/9
3. R.S. Withers, A.C. Anderson, P.V. Wright, and S.A. Reible, *IEEE Trans. Magn.* **MAG-19**, 480 (1983).
4. R.S. Withers, A.C. Anderson, J.B. Green, and S.A. Reible, *IEEE Trans. Magn.* **MAG-21**, 186 (1985).
5. R.S. Withers and P.V. Wright, *Proc. 37th Annual Symposium on Frequency Control* (IEEE, New York, 1983), p. 81.
6. M.A. Delaney, S.M. Thesis, MIT Dept. of Materials Science & Engineering (1986).
7. J.J. Hopfield, *Proc. Natl. Acad. Sci. U.S.A.* **79** (Biophysics), 2554 (1982).
8. J.P. Sage and P.M. Grant, in *Amer. Inst. Phys. Conf. Proc., Neural Networks for Computing*, 1986.
9. Solid State Research Report, Lincoln Laboratory, MIT (1986:1), p. 51.
10. T. Kohonen, *Self-Organization and Associative Memory* (Springer-Verlag, Berlin, 1984).

UNCLASSIFIED

SECURITY CLASSIFICATION OF THIS PAGE (When Data Entered)

REPORT DOCUMENTATION PAGE		READ INSTRUCTIONS BEFORE COMPLETING FORM
1. REPORT NUMBER ESD-TR-86-099	2. GOVT ACCESSION NO.	3. RECIPIENT'S CATALOG NUMBER
4. TITLE (and Subtitle) Solid State Research		5. TYPE OF REPORT & PERIOD COVERED Quarterly Technical Report 1 May — 31 July 1986
		6. PERFORMING ORG. REPORT NUMBER 1986:3
7. AUTHOR(s) Alan L. McWhorter		8. CONTRACT OR GRANT NUMBER(s) F19628-85-C-0002
9. PERFORMING ORGANIZATION NAME AND ADDRESS Lincoln Laboratory, MIT P.O. Box 73 Lexington, MA 02173-0073		10. PROGRAM ELEMENT, PROJECT, TASK AREA & WORK UNIT NUMBERS Program Element No. 63250F Project No. 649L
11. CONTROLLING OFFICE NAME AND ADDRESS Air Force Systems Command, USAF Andrews AFB Washington, DC 20334		12. REPORT DATE 15 August 1986
		13. NUMBER OF PAGES 82
14. MONITORING AGENCY NAME & ADDRESS (if different from Controlling Office) Electronic Systems Division Hanscom AFB, MA 01731		15. SECURITY CLASS. (of this Report) Unclassified
		15a. DECLASSIFICATION DOWNGRADING SCHEDULE
16. DISTRIBUTION STATEMENT (of this Report) Approved for public release; distribution unlimited.		
17. DISTRIBUTION STATEMENT (of the abstract entered in Block 20, if different from Report)		
18. SUPPLEMENTARY NOTES None		
19. KEY WORDS (Continue on reverse side if necessary and identify by block number)		
solid state devices	photodiodes	electro-optic devices
quantum electronics	lasers	charge-coupled devices
materials research	laser spectroscopy	acoustoelectric devices
microelectronics	crystal growth	microwave semiconductor devices
analog device technology	signal processing	superconductive devices
20. ABSTRACT (Continue on reverse side if necessary and identify by block number)		
<p>This report covers in detail the solid state research work of the Solid State Division at Lincoln Laboratory for the period 1 May through 31 July 1986. The topics covered are Solid State Device Research, Quantum Electronics, Materials Research, Microelectronics, and Analog Device Technology. Funding is provided primarily by the Air Force, with additional support provided by the Army, DARPA, Navy, SDIO, NASA, and DOE.</p>		